Hydrodynamics of countercurrent flow in an additive manufactured column with triply periodic minimal surfaces for carbon dioxide capture

Rajesh Kumar Singh[1*], Yucheng Fu[1], Chao Zeng[1], Du Thai Nguyen[2], Pratanu Roy[2], Jie Bao[1], Zhijie Xu[1] and Grigorios Panagakos[3]

[1]Pacific Northwest National Laboratory, Richland, WA 99352, USA;

[2]Lawrence Livermore National Laboratory, CA 94550, USA;

[3]Carnegie Mellon University, Pittsburgh, PA 15213, USA

*Corresponding Author: rajesh.singh@pnnl.gov; rajeshsingh.175@gmail.com

ABSTRACT

Computational investigation of the countercurrent flows in an additive-manufactured (AM) column packed with triply periodic minimal surface (TPMS) is challenging. Multiphase flow simulations using the volume of fluid (VOF) method can explain the column's hydrodynamic characteristics, including interfacial area, liquid holdup, pressure drop, flow regime, etc. The interfacial area is a key factor dictating the mass transfer via the absorption process, and thereby the overall efficiency of the column. The impacts of a solvent's physical properties, liquid and gas loads, and contact angle on the hydrodynamics are extensively explored. The solvents include traditional solvent (monoethanolamine [MEA]) used in industry as well as a water-lean solvent (EEMPA) as prospective solvents for carbon capture. As expected, interfacial area and liquid holdup increase with increasing liquid loads (q_L). The EEMPA exhibits higher values for the interfacial area and liquid holdup compared to those for the MEA. The dry and wet pressure drops per unit length in the column at different gas loads (F_G) are calculated and further compared with the empirical correlations for traditional packings. At low gas loads, i.e., in the preloading regime, the predicted values of the wet and dry pressure drops match well with the corresponding values calculated from available correlations. The gas load has a marginal impact on the interfacial area at its lower value, but the higher value of F_G ($> 2.18\sqrt{Pa}$) causes flooding in the column. The effect of varying contact angles on the interfacial area and liquid holdup in the preloading regime is also studied. Both interfacial area and liquid holdup decrease with the increase in the value of the contact angle. Overall, the effect of the contact angle on the interfacial area is more pronounced than other parameters influencing the interfacial area.

Keywords: Additive-manufactured column, contact angle, interfacial area, liquid holdup, pressure drop, column flooding

1. Introduction

Anthropogenic greenhouse gas (GHG) emissions to the atmosphere, primarily sourced from the combustion of fossil fuels such as coal, hydrocarbon, natural gas, and petroleum for energy generation, contribute to global warming and climate change [1]. GHG absorbs energy from infrared radiation and traps heat in the lower atmosphere, which can cause global warming [2]. Carbon dioxide (CO_2)- emissions from the combustion of fossil fuel contributed approximately 75% of the total U.S. GHG emission in 2018 [1]. Post-combustion CO_2 capture has gained significant attention in recent decades and is being explored as a prospective technology for reducing emissions from power plants to mitigate the adverse impacts of global warming [3-5]. Post-combustion carbon capture via absorption could be economical and efficient because it can be readily retrofitted in the existing power plant. Traditional packed columns— structured packing, random packing, etc.—are currently being explored and their performance and scalability for industrial deployment need to be carefully evaluated [6]. Over recent decades, computational fluid dynamics (CFD) has gained significant attention for its use in exploring the hydrodynamic characteristics and mass transfer of packed columns. It economically and efficiently provides insights into flow through packed columns and thereby complements the conduct of tedious experiments. Because of the existing wide range of length scales and flow regimes, multiphase flow simulations in the column are a multiscale problem [7]. The hydrodynamics of a column depend on various factors, including solvent properties, liquid and gas loads, the packing surface features (texture, roughness, etc.), and the packing characteristics (porosity, surface area, main particle diameter or hydraulic diameter, etc.). An enhanced understanding of the hydrodynamics would be useful in optimizing the design and operation of a packed column.

Additive manufacturing (AM), also known as 3-D printing by layer-by-layer fabrication [8], has emerged as a promising technology for innovation in many engineering and natural processes because of its associated precise and controlled 3-D geometry [9-11]. It offers various advantages over traditional manufacturing for designing tailored and optimized structures, and subsequently improving associated heat and mass transfer efficiencies [12]. In addition, AM techniques possess a several advantages such as wide range of material's variability and the manufacturing parameters for achieving an optimal design. For an absorber design, AM offers more flexibility in design optimization for enhancing the gas-liquid interface and increasing absorber column efficiency [10, 13]. Interests in exploring the benefits of AM for designing packed columns for the absorption process [12, 14, 15] have also been raised over the couple of decades. In addition to the application of AM in to modifying the design of traditional packings, novel packing design is being explored for process intensification of packed columns. A triply periodic minimal surface (TPMS) can be used for absorption and simultaneous heat transfer [16]. TPMS is deemed ideal for cell adhesion, migration, and vitalization in tissue engineering, because it has several desirable characteristics such as a smooth surface, higher specific area, and excellent permeability [17, 18]. The TPMS geometry can enhance the mass transfer without causing a significant increase in the pressure drop; consequently, it becomes a good choice for use in ultrafiltration systems [19]. A wide range of TPMS structures can be mathematically developed and fabricated using AM, commonly known as 3-D printing. The generated TPMS structures may have two spatially disconnected flow domains intertwined in intimate contact [16]. As depicted in Figure 1(a), configurations of a TPMS having design of Schwarz-D surface (design parameter described later) have various disconnected flow channels, which can be used simultaneously for heat and mass transfer. If Schwarz-D surfaces are used as packing elements in the absorption column, one domain could contain the countercurrent gas and liquid flow, while other one carry the heat exchanger fluid to control the temperature of the absorber [20]. Furthermore, Schwarz-D surface can also be used as a traditional packed column if both volume domains are used for gas absorption [16]. The advantage of TPMS geometry is that it has a higher specific area at higher value of porosity of the column [21].

As mentioned earlier, interfacial area is a key parameter for absorption process, and the maximum possible interfacial area is desirable to enhance the column efficiency. The interfacial area generally reflects solvent flow patterns within the column. Several studies [22-28] have investigated the interfacial area in packed columns. Janzen et al. [29] explored the impact of viscosity on liquid holdup and interfacial area in MellapakPlus 752.Y packing. Both quantities increase with the increased value of viscosity and solvent flow rates. However, Tsai et al. [30] showed that solvent viscosity has a negligible effect, whereas surface tension marginally affects the interfacial area. Furthermore, enhanced solvent viscosity leads to increased film thickness [31] and reduced solvent diffusivity [32, 33]. Flow simulations were conducted in the representative elementary unit (REU) of the packed columns [25, 26, 34-37]; doing so replicated the identical hydrodynamic characteristics of the packing unit while requiring minimum computational resources. Recent multiphase studies in the REU of Gempak 3A [25] were conducted to develop correlations for the interfacial area and liquid holdup in a packed column. The interfacial area initially increases with increased liquid load then achieves a net value [25]. Furthermore, the gas flow rate has a negligible impact on the interfacial area in loading and preloading regimes [38-40]. In addition, wetting in a packed column is also dictated by the packing surface characteristics by the solid-liquid system energetics [41] represented by surface roughness, texture, and contact angle. The contact angle is a complex parameter that depends on various factors such as the solid-liquid systems in a specific environment [42, 43], the surface texture of the packing material [44, 45], the packing material [46, 47], and the surface tension of the solvent [47]. A smaller value of contact angle leads to increased interfacial area [31, 48]. The impact of contact angle on interfacial area is tied to the surface tension of the solvent [31, 46]. The contact angle has a pronounced effect on the interfacial area for a solvent that has a lower surface tension [25, 48].

The hydrodynamics of additive-manufactured column is quite complex. The impact of the various parameters on the hydrodynamics in the novel packing with TPMS is not yet fully understood. A few studies have focused on the small periodic cells of the TPMS, but they were limited to single-phase flow for dry pressure drop calculation in the small periodic cell [21, 49]. Recent studies [16, 50] have demonstrated a process design that uses heat exchanger within an absorber thereby controlling the temperature of column. The novel design could be promising for intensifying heat removal and recovery in absorption columns. Indeed, further studies were recommended for improved packing designs for, and applications to, other industrial processes. Accordingly, this present study investigates the countercurrent flows in the AM column packed with Schwarz-D surface. Outcome of the present study would be helpful in the understanding the hydrodynamics of the packed column while designing the optimum absorption using AM.

In this paper, the hydrodynamics of countercurrent flows in the Schwarz-D column are extensively investigated. The mathematical formulation is described in Section 2. The method and material presented in Section 3 briefly describes problem setup, meshing, and numerical scheme used in the flow simulation. In Section 4, we investigate in detail the impacts of various parameters—liquid load, gas load, contact angle, etc.—affecting the interfacial area, liquid holdup, and pressure drop in the packed column. The comparison of predicted liquid holdup with corresponding experimental observations is presented. Finally, we offer conclusions of the present studies.

2. Mathematical formulations

Flow simulations for the hydrodynamics of countercurrent flows in the Schwarz-D packed column using AM were conducted using STAR-CCM+ [51]. The turbulent multiphase flow simulations were conducted using the volume of fluid (VOF) method [52]. The governing equations for the VOF method are as follows:

$$\nabla \cdot \mathbf{u} = 0, \tag{1}$$

$$\frac{\partial(\rho\mathbf{u})}{\partial t} + \nabla \cdot (\rho\mathbf{u}\mathbf{u}) = -\nabla p + \mu\nabla \cdot \left(\nabla\mathbf{u} + \left(\nabla\mathbf{u}\right)^T\right) + \rho\mathbf{g} + \mathbf{F}, \tag{2}$$

where, $\mathbf{u}$ is the velocity, p is the pressure, $\boldsymbol{g}$ is the gravity, and $\mathbf{F}$ is the interfacial tension force that produces a normal pressure jump across the interface. The terms ρ and μ are the phase-averaged values of density and viscosity, respectively.

The interfacial force ($\mathbf{F}$) appearing at the gas-liquid interface is implemented by the continuous surface force model [53]:

$$\mathbf{F} = \sigma \frac{\rho\kappa\nabla\alpha}{\frac{1}{2}\left(\rho_G + \rho_L\right)} \tag{3}$$

where σ is the surface tension value; κ is the local curvature of the interface; α is the volume fraction of the primary phase; subscripts L and G denote the liquid and gas phases, respectively; and $\nabla\alpha$ is the gradient of the volume fraction representing the direction vector at the gas-liquid interface. The curvature κ is computed as the divergence of the unit normal ($\hat{n} = \nabla\alpha/|\nabla\alpha|$):

$$\kappa = \nabla \cdot \hat{n} \tag{4}$$

The interface where two fluids meet the solid surface is computed using wall adhesion and the contact angle (γ). The normal vector at the interface is adjusted near the wall by the following equation:

$$\hat{n} = \hat{n}_{wall} \cos\gamma + \hat{t}_{wall} \sin\gamma \tag{5}$$

where, $\hat{n}_{wall}$ and $\hat{t}_{wall}$ are the unit vectors normal and tangential to the wall, respectively.

The interface between the phases is captured by solving transport Equation (6) for the volume fraction of the secondary phase (α) that varies in the range of 0 to 1:

$$\frac{\partial \alpha}{\partial t} + \nabla \cdot \mathbf{u}\alpha + \nabla \cdot \mathbf{u}_c \alpha(1-\alpha) = 0 \tag{6}$$

where, u_c is the sharpening velocity computed as $C \times |\mathbf{u}|\, \nabla\alpha/|\nabla\alpha|$, C is the sharpening factor. The last term on the left side of Equation (6) is only active in the region proximate to the interface; it reduces the artificial numerical diffusion to ensure a sharp interface.

2.2 Turbulence modeling

The flow in the packed column is assumed to be turbulent because of its complex geometry, and flows inside the packed column deviate from the well-known reference cases [54]. Thus, additional closures are required to model turbulence in the turbulent flow simulation. The two-equation standard k–ε turbulence model fails to accurately predict flow characteristics in a structured packing [55-57]. Hence, the two-equation Shear Stress Transport (SST) $k - \omega$ turbulence model [58] is used, because it is more suitable for studying separated, reversed, and recirculating flows. The transport equations for turbulence are as follows:

$$\frac{\partial(\rho k)}{\partial t} + \frac{\partial(\rho u_j k)}{\partial x_j} = P - \beta^* \rho\omega k + \frac{\partial}{\partial x_j}\left[(\mu + \sigma_k \mu_t)\frac{\partial k}{\partial x_j}\right] \tag{7}$$

$$\frac{\partial(\rho\omega)}{\partial t} + \frac{\partial(\rho u_j \omega)}{\partial x_j} = \frac{\gamma}{\nu_t} P - \beta\rho\omega^2 + \frac{\partial}{\partial x_j}\left[(\mu + \sigma_\omega \mu_t)\frac{\partial \omega}{\partial x_j}\right] + 2\rho(1-F_1)\frac{\sigma_{\omega 2}}{\omega}\frac{\partial k}{\partial x_j}\frac{\partial \omega}{\partial x_j} \tag{8}$$

where, P is the production rate of the turbulent kinetic energy due to the mean velocity gradient and is calculated as follows:

$$P = \tau_{ij} \frac{\partial u_i}{\partial x_j} \tag{9}$$

where, $\tau_{ij} = 2\mu_t S_{ij}$ and $S_{ij} = \frac{1}{2}\left(\frac{\partial u_i}{\partial x_j} + \frac{\partial u_j}{\partial x_i}\right)$

α_k and α_ε are the inverse of effective turbulent Prandtl numbers for the k and ε equations, respectively. The eddy viscosity is computed as:

$$\nu_t = \frac{a_1 k}{\max\left(a_1 \omega_1, \Omega F_2\right)} \tag{10}$$

where, $\Omega = \sqrt{W_{ij} W_{ij}}$ is the voracity magnitude and $W_{ij} = \frac{1}{2}\left(\frac{\partial u_i}{\partial x_j} - \frac{\partial u_j}{\partial x_i}\right)$. The model empirical constant values used are the default ones suggested by Menter [58].

3. Material and methods

Hermann Schwarz first described a TPMS [59] that has constant mean curvature throughout the surface and that is periodic in all directions. The Schwarz-D surface does not have self-intersections and it was named “diamond” because its symmetries are related to the diamond crystal. Schwarz-D could be a promising structure manufactured via 3-D printing in many engineering applications because it has higher porosity and a large surface area per unit volume [60]. The surface of the Schwarz-D can be mathematically designed using Equation (11):

The Schwarz-D packing surface was mathematically generated using Equation (11), then a computer-aided design (CAD) model of the packing element was exported in a stereolithography (stl) file. The Schwarz-D packing is 76.2 mm in diameter and 50 mm in height. Average wall thickness of the Schwarz-D is 0.4 mm, and it can be precisely created using AM technique. Subsequently, the specific area ($a_p = A_p/V_p$, A_p and V_p are Schwarz-D surface area and geometric volume of column) and porosity of the column ($\epsilon = V/V_p,\ V$ is void volume) of the Schwarz-D column are found to be $620\ m^2/m^3$ and 0.89 respectively. It shows the advantage of schwarz-D column over traditional structured packed column since a higher specific area can be achieved in the present case. Based on these parameters, the hydraulic diameter of the packed column ($d_h = 4\epsilon/a_p$) is found to 5.76 mm. The CAD model of the packing element was imported in STAR-CCM+ for development of a model of the computational flow domain. The flow domain has a cylindrical shape and is 80 mm in diameter and 75 mm in height (see Figure 1(b)). The size of the cylinder was considered larger than the size of the packing element to specify smooth boundary conditions for stable and converged simulations. However, simulation results were only be analyzed in the packing element. The packing element was placed in the center of the cylinder and solvent was fed into the column through the distributor (see Figure 1(c)). The liquid distributor contains 27 dripping points and is 4 mm in diameter, same as the experimental setup for earlier absorber column experiments [61], and 15 mm in length (small cylinders with red and grey colors in Figure 1(c)). These dripping points feed solvent in both channels of packing that was confirmed by solvent distribution at different planes in column (discussed in later section). Next, the meshing of the domain is a critical step that affects the stability of simulations and the accuracy of the results. To capture the hydrodynamics accurately and efficiently, the flow domain was discretized using nonuniform mesh (Figure 2). As shown in the exploded view of the mesh in the cross-sectional plane of the column in Figure 2a, the mesh near the surface of the packing element and column wall was created to be very fine using a prism layer meshing scheme (equivalent to boundary layer meshing). In this region, liquid film is expected to appear, and interphase transport phenomena occur; consequently, a very fine mesh is needed to resolve the physics accurately. Therefore, a minimum grid size of 10 μm was specified in the prism layer region. Then, gradient-based polyhedral mesh was used to discretize the remaining part of the column. Subsequently, the size of the grids proximate to the prism layer was assigned to be smaller than the mesh in the centerline of the Schwarz-D elements (see Figure 2). Note that the core region of the Schwarz-D channels does not actively contribute to the transport phenomenon of interest, so coarse mesh was used in that region. The optimum number of cells in the flow domain was determined after conducting the grid convergence study. The results for the grid convergence test are discussed in a later section.

Table 1: Physical properties of solvents used in flow simulations at 25°C.

Solvent	$\boldsymbol{\rho_L}$ (kg/m^3)	$\boldsymbol{\mu_L}$ (mPas)	**σ** (mN/m)	**Ka**
Water	997	0.97	72.80	3538
40MEA (40% MEA by weight)	1053	3.791	54.80	443
EEMPA	938	7.083	34.40	116

Commercially used aqueous amines-based solvents contain 70–50% w/w water for carbon capture. The water content in the solvent adversely impacts the solvent's working capacity, thermal regeneration energy, and solvent circulation rates [62]. To overcome these issues, several capture materials—hydrophobic amines, CO_2-binding organic liquids (CO_2BOL), functionalized-ionic liquids, and amine/organic solvent mixtures for solvent—are currently being developed, and they have low water contents [63]. Pacific Northwest National Laboratory (PNNL), with industrial collaboration, has developed a water-lean solvent CO_2BOL as an alternative to the energy-intensive aqueous-amine solvents used for carbon capture [64, 65]. EEMPA [N-(2-ethoxyethyl)-3-morpholinopropan-1-amine] is among the well-characterized CO_2BOL derivatives that overcome past viscosity challenges observed in its previous derivatives [66]. Still, the water-lean solvent is in the development stage, and comprehensive investigations are required to assess its performance for post-combustion CO_2 capture at an industrial scale. Multiphase flow studies were conducted using flue gas (ρ_G = 1.185 kg/m^3 and μ_G = 1.831×10^{-5} Pa.s) and different solvents. The solvents included water, aqueous solutions of MEA at 40% by weight concentrations (40MEA), and EEMPA. The physical properties of these solvents are presented in Table 1. The contact angle (γ) value for each solvent was not available. Note that the CO_2 absorption is carried out in the pre-wetted column in which the surfaces of the packing material are non-planar, textured, and heterogeneous. Under this condition, one can expect a lower value of the contact angle. For this reason, the effects of contact angle on the interfacial area and liquid holdup were systemically studied.

The unsteady flow simulations were conducted using implicit transient formulation, which involved inner iterations in a time step for converged solution. The coupling of the momentum and continuity equations was achieved by using a predictor-corrector approach in conjunction with the SIMPLE (Semi-Implicit Method for Pressure-Linked Equations) algorithm [56] for pressure-velocity coupling. The second-order upwind scheme was utilized in the discretization of all equations. The simulation used the implicit solution scheme in conjunction with algebraic multigrid method for accelerated convergence. HRIC (high-resolution interface capturing), an efficient method to capture sharp interface, was used in the discretization of transport equation for volume fraction [57]. Flow simulations were terminated when the wetted and interfacial areas in the column achieved the pseudo-steady state. The flow simulations required a very small time step ($\boldsymbol{\Delta t \sim 10^{-5} - 10^{-4}\ sec}$) to achieve a stable and converged solution. Consequently, flow simulations were very expensive; e.g., a single simulation took 4–6 days of wall-clock time, depending upon the solvent properties and contact angle, using 192 cores to achieve the pseudo-steady state.

4. Results and discussions

The simulation results for predicting the dry pressure drop, interfacial area, and liquid holdup are discussed below. The grid convergence test is reported first to ensure the accuracy of the CFD prediction. The predicted value of the liquid holdup is compared with the corresponding experimental columns using the Schwarz-D packings. Further, the effects of the various parameters—liquid load, gas loads, solvent properties, and contact angles on the interfacial area, liquid holdup, and pressure drop across the column—are presented and explained.

4.1 Grid convergence test

The grid convergence test is a prerequisite for numerical studies that aid in estimating the optimal number of cells in the computational flow domain for conducting efficient and economic simulations. A coarser grid resolution can lead to unstable simulations and inaccurate results, while a very fine grid leads to a large number of cells, and a very small time step is required to achieve a stable and converged solution. Consequently, flow simulations become computationally very expensive. For this reason, flow simulations were initially performed for EEMPA at $q_L = 180\ m^3/m^2h$, $\gamma = 30°$ and six grid resolutions to obtain a reasonable number of cells in the flow domain for efficient and accurate simulation. The gas-liquid interface was generated as the iso-surface that corresponds to $\alpha = 0.50$ [11, 18, 40]. Figure 3(a) shows the wetting process in the column as the temporal evolution of gas-liquid interface. As seen in Figure 3(a), multiphase flow simulations were started with initially dry column and solvent starts falling over the packing surface to wet the column. Rivulets and droplets are observed in the intermediate time (t = 0.20 – 1.50 sec). With progress of time, solvent reaches the bottom and exits from the bottom (t = 2.0 sec). Consequently, simulation achieves pseudo steady state. Next, the area of the interface (A_I) was computed and further normalized by A_p as $A_{In} = A_I/A_p$. The optimum number of cells was established based upon the value of A_{In} at these grid resolutions. Figure 3 shows the temporal evaluation of A_{In} for these cases. As expected, A_{In} first increases with time and then achieves a net pseudo-steady value for all cases. The pseudo-steady value of A_{In} converges with the increased number of cells, i.e., enhanced grid refinement. The intermediate grid resolution of 6.65 M cells was chosen for further simulations. Although there is a slight deviation in the value of $A_{In}(= 0.38)$ at this grid resolution, the shape of the interface does not significantly differ from that at 8.17 M cells ($A_{In} = 0.36$) (see inset in Figure 3). The discrepancy in the pseudo-steady value of A_{In} is within the reasonable limit $(\sim 5\%)$. The chosen grid resolution (6.65 M cells) took 3 days of wall-clock time on 144 cores to achieve a pseudo-steady state, while the finest resolution (8.17 M cells) took almost a week.

4.2 Comparison with liquid holdup against experiments

Preliminary flow simulations were conducted to validate the numerical methods that reflect the extent of accuracy. To ensure the reliability of the current simulations, the predicted results are qualitatively and quantitatively compared with those obtained from the experiments conducted as part of this effort. Indeed, validation of numerical methods is a prerequisite for any numerical study.

A 3-D printed packing section based on the Schwarz-D TPMS geometry was fabricated using a Form 2 SLA 3-D printer and the Clear FLGPCL04 resin. This method of 3-D printing uses stereolithography (SLA) to manufacture the structure, which produces precise parts. The initial Schwarz-D surface was generated in MathMod, an inteactive plotting and graphing program specialized for surfaces based on implicit functions, such as TPMS geometries. The surface file was then imported into the computer graphics software Blender, where the desired geometriec properties and thickness were added to the surface. The printed structures of the Schwarz-D packing has surface thickness of 2 mm and specific surface area of 250 m^2/m^3. The outer diemsion of Schwarz-D column has a height of 150 mm and a diameter of 75 mm.

Liquid holdup measurements were conducted for the Schwarz-D packings based on a volumetric approach adopted by Niegodajew et. al [67]. A general schematic of the experimental setup can be found in Figure 4(a). The static liquid holdup was determined by first measuring the initial mass of the packings. The packings were then flooded with excess water, after which the excces water flow was shut off. The column was allowed to drain until the time interval between single drops exceeded 30 seconds. The mass of the column and remaining water mass were then measured to obtain the static holdups. For dynamic holdups, water was fed from the top of packings using a single inlet at high liquid loads to fully wet the packings (see Figure 4(b)). Afterward, the water velocities were reduced to the desired liquid velocities and allowed to flow through the column until the water was stabilized. The water feed was then shut off and the remaining water was allowed to drain into a container until it stopped dripping, and, again, the time between single drops was longer than 30 seconds. The resulting mass of the drained water in the collection tank was measured and it corresponded to the dynamic holdup. The column was dried between each trial. The total holdup value was the combined static and dynamic holdup values.

Consistent with experiments, flow simulations were conducted for water as a working fluid. Air was initially considered the stagnant phase. The water was injected into the flow domain via a small section diameter of 25 mm and was located slightly above the column (see the region enclosed by the dark gray wall in Figure 5(c)). Based on the experimental measurement of the contact angle for AM column material (Clear FLGPCL04), a 70° static contact angle was prescribed at the column surface. Flow simulations were conducted using liquid loads specified by the experiments. Consistent with the experimental setup, the liquid load was defined in different way and described based the column cross-section area. Further, the liquid holdup (h_L) was computed as the fraction of the column's volume occupied by solvent as $h_L = V_L/V_p$, where V_L and V_p are the entrained solvent and geometric volumes, respectively. As shown in Figure 5(a), the liquid holdup in the computational flow domain initially increases and then achieves a net pseudo steady value. Therefore, simulations were conducted for a sufficiently long time to achieve a pseudo-steady state for the liquid holdup in the column at each liquid loads (see Figure 5(a)). Once flow achieved the pseudo-steady state, value of the liquid holdup was computed only in the region that contains TPMS packing. Consequently, slightly higher value of the liquid holdups is arrived, and compare with the corresponding experimental results in Figure 5(b). Note that blue circles in Figure 5(b) represent the pseudo-steady value of liquid holdup of each liquid load. As expected, liquid holdup increases with increased liquid load. This behavior can also be observed in the snapshot of the gas-liquid interface (defined as the iso-surface corresponding to $\alpha = 0.50$) at different liquid loads shown in Figure 5(c). With increased liquid load, transition of the flow regimes rakes place, droplet to rivulet and then partially film regime. As shown in Figure 5(b), the predicted value of the liquid holdup matches well with the experimental value at the lower liquid load. At the higher liquid load, there is a slight discrepancy between the values, but otherwise they show good agreement. The discrepancy in the liquid holdup might be due to uncertainty in the experimental conditions and contact angles approximation. Note that at higher value of water flow rate, static contact angle has limitation to predict the contact line motion in water and solid substrate interaction. Otherwise in the lower range of water flow rate, a good agreement of the value of liquid holdup is seen in both methods.

Indeed, the validation of the current simulation framework using the VOF method for countercurrent flow has been successfully performed for various applications [31, 46, 61, 68-70]. The VOF-predicted wetted area and film thickness compared well with the experimental results and analytical theory for film falling over inclined plates [15]. Next, the VOF simulation for dynamic instability and breakup of rivulet flows was also validated with an in-house experiment conducted at PNNL [68, 70]. In subsequent studies [46], predicted wetting of a textured corrugated sheet of Montz B1-300 packing was found to compare well with corresponding experiments by Subramanian and Wozny [71]. In recent studies, the CFD-predicted hydrodynamics of random packed columns were validated against in-house experimental observation of device-scale absorber columns [61]. In addition, the VOF method was validated for its use in investigating the reactive mass transfer in two-phase flow [32, 72, 73]. Therefore, the VOF multiphase method can be an appropriate tool for investigating the countercurrent flows in an additive-manufactured packed column.

4.3 Dry pressure drop in the column

The dry pressure drop across the column was computed and further compared with the value calculated from the empirical correlation for the dry pressure drop in a packed column [74, 75]. The dry pressure drop per unit column height is given as

$$\frac{\Delta p_0}{H} = \psi_0 \frac{1-\varepsilon}{\varepsilon^3} \frac{F_G^2}{d_p} \frac{1}{K} \tag{12}$$

where, F_G is the gas capacity factor computed as $F_G = u_G \sqrt{\rho_G}$, ψ_0 is the resistant coefficient

$$\psi_0 = \frac{160}{\mathrm{Re}_G} + \frac{3.1}{\mathrm{Re}_G^{0.1}} \tag{13}$$

where Re_G is the gas-phase Reynolds number depending on particle diameter, d_p, and is computed as $\mathrm{Re}_G = u_G d_p K / \{(1-\varepsilon)\nu_G\}$. The particle diameter d_p depends on the porosity (ε) and specific area (a_p) of the column and is computed as $d_p = 6(1-\varepsilon)/a_p$. K is the wall factor that accounts the additional free space at the wall of the column, and is computed as follows:

$$\frac{1}{K} = 1 + \frac{2}{3} \frac{d_p}{(1-\varepsilon)D} \tag{14}$$

Note that the local void fraction differs from the theoretical value depending upon the overall diameter of packed column, D. The column has a small diameter subsequently, and K can play a significant role in the pressure drop calculation in dry packing. For columns of small diameters, the wall effects increase significantly [76].

For the structure packed column, the value of ψ is given by Stichlmair et al. [77] and calculated as

$$\psi_0 = \frac{C_1}{\mathrm{Re}_G} + \frac{C_2}{\mathrm{Re}_G^{0.5}} + C_3 \tag{15}$$

The values of C_1, C_2, and C_3 depend on the packing design and sheet material. For metal sheet Mellapak 250.Y packing, the value empirical constants were found to be $C_1 = 5$, $C_2 = 3$, and $C_3 = 0.45$ [77].

The area-weighted average pressure was calculated in the cross-sectional planes 4 mm below and above the packing element. These values were used to calculate the pressure drop across the column, and the pressure drop was divided by the separation between these planes. Figure 6 plots the variation of the dry pressure drop per unit length ($\Delta p_0\ /H$) with F_G^2. As expected, the dry pressure increases with the increased value of F_G^2. Similar behavior was also observed for the periodic unit of Schwarz-D packing [21]. The predicted value of the dry pressure drop matches well with the theoretical value (12) and Ergun equation [78] at the lower F_G^2 value. At higher value of gas capacity factors, all expressions show higher values. Note that the Ergun model for dry pressure drop is valid at a lower Reynolds number, and hence at the lower gas load capacity. The predicted value of ($\Delta p_0\ /H$) was also compared with the pressure drop across the Mellapak 250.Y column using the Stichlmair model [77]. The pressure drop in the Schwarz-D column shows a higher value than the corresponding one for Mellapak 250.Y at all gas loads investigated. This was expected because the Schwarz-D TPMS structure has more flow resistance, particularly attributed to the turn and twist in the flow path.

4.4 Effect of liquid loads and solvent properties

The multiphase flow simulations were conducted for a wide range of liquid loads ($18–250\ m^3/m^2h$) at $\gamma = 10°$, $F_G^2 = 1.18\ Pa$ and for three solvents (see **Error! Reference source not found.** for the physical properties of the solvents). The countercurrent flow in the Schwarz-D column is presented in Figure 7(a) in which color contours depicted the downward solvent flow. The velocity vector plot shows the upward gas flow. The liquid load is defined as solvent flow rate per unit area of dripping points. The dripping points feed the solvent into both channel that can be confirmed by the solvent distribution in a cross-section of column located at the middle of column in Figure 7 (b). The flow simulations were initially conducted at a fixed F_G^2 value based on previous studies for countercurrent flow in structure [25, 68] and random [27] packed columns. The impact of the gas load factor on the hydrodynamics is extensively explained in a later section. The effects of physical properties and liquid loads on both liquid holdup and normalized interfacial area are discussed here.

As mentioned earlier, the local hydrodynamics of a packed column depends on the physical properties of the solvent. The interfacial area is a key parameter dictating the interphase mass transfer in an absorption system that can be assessed accurately. The interface is the surface that distinguish gas and liquid regions, and absorption reaction takes place there. The wetted surface is the portion of solid substrate that is direct contact with liquid, and corresponding area of the that region is represented as wetted areas (A_W). The wetted area does not actively participate the interphase mass transfer process. Further, direct and indirect methods were applied to estimate the interfacial area (effective mass transfer area) in the packed column. The indirect method for measuring the effective mass transfer area in the experiments used the Danckwerts method [79], which is based on the absorption of CO_2 into aqueous caustic solvents in instantaneous irreversible reactions. The interfacial area was calculated from the absorption data using estimates for the mass transfer coefficients [38, 80]. In contrast, the interfacial area can be directly computed as the area of the iso-surface with $\alpha = 0.50$ in the flow simulation. The shape of the gas-liquid interface is shown in the inset of Figure 7(c) for EEMPA. A similar approach was also adopted earlier for the calculation of interfacial area [22, 26, 46]. The computed value of the interfacial area ($\mathrm{A_I}$) was normalized by the specific area of the packing ($\mathrm{A_p}$) as $A_{In} = A_I/A_p$. Further, the simulations were conducted for a sufficiently long time to achieve a pseudo-steady state for the wetted and interfacial areas in the column (see Figure 7(c)). Once the flow achieved a pseudo-steady state, the interfacial area was computed and further analyzed.

Flow simulations were conducted for water-lean solvent and a traditional aqueous solvent used in the carbon capture at a given contact angle (see Table 1). Figure 8(a) shows the variation of the interfacial area with the liquid loads for these solvents at a lower value of contact angle, $\gamma = 10°$. As expected, the interfacial area increases with the increased value of the liquid load. At a low liquid load, the interfacial area increases quickly, then the interfacial area grows slowly with further increases in the liquid load. This behavior is somewhat expected. In the case of the structured and random packed columns, the interfacial area becomes insensitive to the liquid load in the higher liquid load range [25, 27, 68]. Further, EEMPA shows a higher value of the interfacial area than the other solvents studied. This reflects the impact of the physical properties of the solvent on the interfacial area. Note that the EEMPA has a lower surface tension and higher viscosity value. Singh et al. [25, 68] have observed similar behavior in a structured packed column. They explained the impact of the solvent physical properties in terms of Kapitza number (Ka), a dimensionless representation of the fluid properties [31], which is defined as $\mathrm{Ka} = \sigma(\rho_L / g\mu_L^4)^{1/3}$. A solvent that has high surface tension and low viscosity exhibits a higher Ka value (Ka = 116 and 443 for EEMPA and 40MEA, respectively). They found that the interfacial area decreases with increased Ka values, which is also in agreement with the results presented in this study.

Liquid holdup (h_L) is another important hydrodynamic parameter that dictates the overall performance of the packed column. It actively contributes to the resulting wet pressure drop and effective gas velocity, affecting overall efficiency. Figure 8(b) shows the variation in liquid holdup with liquid loads under the same conditions. As expected, the value of h_L consistently increases with the increasing value of the liquid loads. This is also consistent with previous observations of the variation in liquid holdup with liquid load in structured and random packed columns. Further, EEMPA shows a higher value for the liquid holdup than those found for 40MEA and water.

4.5 Effect of gas loads

The previous countercurrent gas/liquid flow simulations in the packed column were restricted to a fixed gas velocity. Gas velocity has a negligible impact on the interfacial area and liquid holdup in the loading and preloading regime. Flow simulations were conducted for EEMPA solvent at $q_L =$

$180\ m^3/m^2h$, $\gamma = 30°$ and different F_G^2 values. The predicted value of wet pressure drop was calculated and further compared with correlations in the literature.

Figure 9(a) shows the temporal evaluation of the interfacial area (A_{In}) for EEMPA solvent at $q_L = 180\ m^3/m^2h$ and different F_G^2 values. As expected, the interfacial area increases first and then achieves a net pseudo-steady value at the gas load capacity $F_G^2 < 4.74$ Pa. Note that the gas load capacity factor does not have a significant impact on the interfacial area (see Figure 9) in this range of F_G^2. Shape of the interface is observed to very smooth and attached to the packing surface. Solvent continuously exits from the bottom of domain. At $F_G^2 > 4.74$ Pa, the effect of F_G^2 on the temporal evaluation of the normalized interfacial area is also visible in shape of the interface in Figure 10(a). Interface is bit chaotic, and solvent is also stick to the column wall. The higher gas load causes more resistance to the liquid phase falling, subsequently solvent is push toward the column wall. Instability in the interface shows the transition of operating conditions from the preloading regime to the loading regime [34]. Note that gas phase kinetic energy is sufficient to destabilize the liquid film formed over the packing in loading regime. Further increase of F_G^2 gives rise to the onset of the flooding at $F_G^2 \geq 4.74$ Pa. Note that the flooding phenomenon is influenced by the size, type, and packing material of the column [75]. During flooding, the gas-phase pressure prevents the liquid from falling and subsequently exiting from the bottom of column. The flooding phenomenon using multiphase flow simulations in a very short column can be predicted as the column mostly occupied by the gas phase and the least liquid is entrained in the column on the top (see bottom two figures in Figure 10(a)). This behavior was further confirmed by observing the velocity vector plot at the gas-liquid interface. As is evident in the exploded view in Figure 10 (b), the solvent initially starts entraining and then spills from the top of the flow domain, delineating the phenomenon equivalent to flooding condition in the large sized column in experimental studies as well as industrial application. Subsequently, the interfacial area and liquid holdup also decrease with the further increase in the gas capacity factor, which can be observed in Figure 9(b). Flooding in the column is delineated as the region on the right side of the green dotted line in Figure 9(b). In a large sized column employed in experiment/industrial column, a higher value of gas load inhibits the solvents exits from the bottom. Consequently, column get filled with solvents and spills from top of the column. On the other hand, numerical studies in a short representative column can predict the flooding by mostly dried column. The pressure drops rise due to the increased gas capacity factor is attributed to the change in the flow characteristics, and therefore the wet pressure drop is subsequently analyzed to understand the flooding behavior.

Table 2: Correlations for wet pressure drop in the packed column.

Model	Expression for $\left(\Delta p_{wet}/H\right)$	Remark
Billet and Schultes [74]	$f(S)\left(\dfrac{\varepsilon}{\varepsilon-h_L}\right)^{3/2}\dfrac{\Delta p_0}{H}$ Here, $f(S)=\exp\left(\mathrm{Re_L}/200\right)$ and $\mathrm{Re}_L=u_L/a_p\nu_L$, ν_L is kinemetic viscosity. $\Delta p_0/H$ from Equation (12).	Random packed column
Stichlmair model [77]	$\left(1+\dfrac{h_L}{1-\varepsilon}\right)^{(2+c)/3}\left(\dfrac{\varepsilon}{\varepsilon-h_L}\right)^{4.65}\dfrac{\Delta p_0}{H}$ Here, $c=-\left\{\dfrac{C_1}{\mathrm{Re_G}}+\dfrac{C_2}{2\cdot\mathrm{Re_G^{0.5}}}\right\}\dfrac{1}{\psi_0}$, $\Delta p_0/H$ from Equation (12), C_1=5, C_2=3	Structured packed column
Maćkowiak model [81]	$\left(1-\dfrac{2\cdot h_L}{a_p\cdot d_h}\right)^{-5}\dfrac{\Delta p_0}{H}$ $\Delta p_0/H$ from Equation (12)	Irrigation channel model for Random packed column

Similar to the dry pressure drop calculation, area-weighted average pressure was calculated in the cross-sectional planes 4 mm below and above the packing element. Next, the wet pressure drop per unit length of the column ($\Delta p_{Wet}/H$) was calculated at different gas capacity factors. $\Delta p_{Wet}/H$ was further compared with existing correlations presented in Table 2 for the wet pressure drop in random and structured packed columns. As shown in Figure 11, $\Delta p_{Wet}/H$ increases with an increased in the value of F_g at the liquid load of 180 $m^3/\ m^2h$. The predicted value of $\Delta p_{Wet}/H$ matches well with empirical models for wet pressure drop by the Billet and Schultes [74] and Maćkowiak models [75] for the random packed column, and the Stichlmair model [77] for the structure packed column all at $F_G^2 \leq\ 4.74$ Pa. This range of the gas capacity factor shows the preloading and loading regime in a packed column. In this regime, the variation of wet pressure approximately holds a relation $\Delta p_{wet}/H \sim F_G^2$, and represented as red double dot line in the Figure 11. Note that the liquid film, rivulet, and droplets form over the packing surface give rise to liquid holdup (h_L) in the column (see Figure 9(b)). Subsequently, open space for the gas flow in the column is reduced, and that may increase the pressure drop across the column. As is evident in Figure 10 (b), liquid is allowed to spill from the top of the flow domain in the present simulation. Consequently, a reduced value of liquid holdup is observed at the very high gas capacity factor (Figure 9(b)). Further increase of gas loads, column becomes mostly dried and liquid holdup is observed to be negligible. As a result, the pressure drop does not further increase because of the negligible liquid entrainment at the very high gas capacity factor in a short column. Previous studies that investigated flooding in the packed column were restricted to the value of the gas capacity factor that lies on the left side of the dotted green line [82, 83].

To understand the flow instability at the higher F_G^2 value, the two-phase pressure drop was normalized by the hydrostatic pressure as $\Delta p_{wn} = \Delta p_{Wet}/(\rho_L g H)$. The normalized wet pressure drop Δp_{wn} was used to predict the flooding in the column. Hanley [84] showed that the value of Δp_{wn} will be approximately same for all packings within a family at f_L. f_L is the fractional approach to flood at a fixed value of liquid loading, and it corresponds to hydraulic states for packed columns. The column shows $f_L = 1$, i.e., flooding condition at $\Delta p_{wn} = 0.2$ (Figures 9-13 of Ref [84]), for a wide range of packing designs and packing materials. This can be evident in the instability in the temporal evolution of the interfacial area, and the shape of the interface as shown in the Figure 10(a). The instability in the interface shows the onset of the flooding at $F_G^2 = 2.18$, which has a $\Delta p_{wn} = 0.29$, and it can lead to flooding condition in the packed column.

4.6 Effects of contact angle

The flow simulations in the packed column were performed at a fixed value of contact angle, $\gamma = 10°$. As noted previously, the contact angle is a critical factor that dictates the wetting phenomenon in the solid-liquid interaction. As described earlier, a solvent can exhibit a distinct value of the contact angle that depends on the solid surface material. The effect of contact angle on the interfacial area and liquid holdup were extensively studied earlier for a rivulet and film flow over an inclined plate [15], corrugated sheet [40], and an REU of the Gempak-2A structure packing [10]. The dynamic contact angle has a marginal impact on the interfacial area compared to the static contact angle in the REU of Mellapak 250.Y packing [68]. Therefore, simulations were restricted to a static value of the contact angle to explore its impact on the interfacial area (A_{In}) and liquid holdup (h_L) in the Schwarz-D column for EEMPA solvent at two liquid loads: 180 and 90 m^3/m^2h.

The effects of contact angle on the normalized interfacial (A_{In}) and wetted (A_{wn}) areas for EEMPA at $q_L = 180\ \mathrm{m^3/m^2h}$ are presented in Figure 12 (a). As expected, both areas are found to decrease with increasing γ values. Consistent with previous studies of traditional packed columns [31, 46], both wetted and interfacial areas significantly change with varying contact angles. The difference between the wetted and interfacial area values shows nonmonotonic variation with the contact angle. At a low contact angle ($\gamma < 40°$) the wetted area value was found to be higher than the interfacial area value, whereas $\mathrm{A_{wn}}$ shows a lower value than $\mathrm{A_{In}}$ at higher γ values. At lower γ values, the adhesive force dominates the cohesive force of the solvent, and subsequently enhanced wetting is observed (see Figure 12(b)). Further, the value of the interfacial area at $\gamma = 10°$ was found to be five times higher than the corresponding one for $\gamma = 70°$. With a decreasing contact angle ($\gamma \leq 40°$), the liquid exhibits enhanced spreading, and transition of flow regime gradually occurs; i.e., rivulet to film flow. This behavior is consistent with that observed in previous studies [25, 31, 69]. In the case of rivulet flow in the corrugated sheet, the solvent prefers to flow in the channel's valley in all cases. At higher γ values, the liquid does not significantly spread and is constrained in the valley; i.e., the bottom of the concave surface in this case. As a result, a thicker rivulet appears there, and consequently the interfacial area shows a higher value than the wetted area. Note that the interphase mass transfer occurs along the interfacial area represented by the red circles in Figure 12(a).

Further, the effect of the contact angle on the interfacial area was also studied at a lower liquid load, $q_L = 90\ \mathrm{m^3/m^2h}$. The interfacial area decreases with the increased contact angle at both liquid loads (see Figure 13). The transition of the flow regime can be observed in the discontinuity in the curve at $\gamma = 40°$ for both cases. The contact angle shows a more pronounced impact on interfacial area variation. Furthermore, the liquid holdup in the packed column decreases with the increasing contact angle value at the two liquid loads (see inset in Figure 13). A higher value of holdup results in an increased wet pressure drop across the column, thereby adversely impacting the column's efficiency.

5. Conclusion

3-D multiphase flow simulations were conducted to investigate the hydrodynamic characteristics of countercurrent flow in the additive-manufactured column. The packed column was filled with Schwarz-D triply periodic minimal surface. The impacts of the liquid and gas loads, solvent properties, and substrate surface characteristics on the interfacial area and pressure drop in the Schwarz-D packed column were extensively explored. Water, traditional carbon capture solvent, as well as water-lean solvents were used to investigate the hydrodynamics of the additive-manufactured column.

For validation of the flow simulations framework, the predicted value of the liquid holdup in the simulation was first compared with that observed in the experimental studies, and both values reasonably match at different liquid loads in the Schwarz-D column. The interfacial area plays a key role in the interphase mass transfer via chemical absorption. The interfacial area initially increases faster with increased liquid load and then grows slowly. On the other hand, liquid holdup consistently increases with the increasing value of the liquid loads for all solvents studied. The effects of gas load on the hydrodynamics were extensively studied for dry and wet pressure drop across the column. The predicted value of the dry and wet pressure drop across the column were also compared with values computed from existing correlations. The wet pressure drop per unit length of column matches well with available correlations below the loading regime. The dry pressure drop in the additive manufactured (AM) packing shows the intermediate value; i.e., lower than the random packing but higher than the structure packing. Further, the higher value of gas loads leads to flooding in the column. The effect of the surface characteristics on the wetting was studied by implementing the contact angle boundary condition. For a given solvent, the interfacial area and liquid holdup increased with the decreasing contact angle (γ) at a fixed flow rate. These outcomes can advance the understanding of the hydrodynamics of additive-manufactured packed columns. The predicted results of the interfacial area, holdup, and pressure drop would provide insights into potential opportunities in process modeling to evaluate the performance of a packed column filled with TPMS structures.

Acknowledgments

Pacific Northwest National Laboratory is operated by Battelle for the U.S. Department of Energy (DOE) under Contract No. DE-AC05-76RL01830. Lawrence Livermore National Laboratory is operated by Lawrence Livermore National Security, LLC, for the DOE, National Nuclear Security Administration under Contract No. DE-AC52-07NA27344. This work was funded by the DOE Office of Fossil Energy's Carbon Capture Simulation for Industry Impact through the National Energy Technology Laboratory (NETL). The authors acknowledge the valuable inputs of Prof. Debangsu Bhattacharyya at West Virginia University. RKS thanks Dr. Janine Carney at NETL for the discussion shared during manuscript preparation.

Disclaimer

Nomenclature

A_I	: Interfacial area
A_I	: normalized interfacial area
A_p	: Physical area of packing surface
a_p	: Specific area of packed column
A_w	: Wetted area
A_{wn}	: Normalized wetted area
AM	: Additive manufacturing
CO	: Courant number
D	: Column diameter
D_h	: Hydraulic diameter
F_G	: Gas load
g	: Gravitational acceleration
h_L	: Liquid holdup
H	: Height of column
i, j	: Spatial tonsorial index
k	: Turbulent kinetic energy
Ka	: Kapitza number
p	: Pressure
P	: Production rate of the turbulent kinetic energy
q_L	: Liquid load
Re	: Reynolds number
t	: Time
$\mathbf{u}$	: Velocity vector
$\mathbf{u_c}$	: Interface sharpening velocity

Greek symbols

δ_{ij}	: Kronecker delta
ε	: Porosity of column
γ	: Contact angle
∇	: Gradient operator

Δt : Time step

Δp_0 : dry pressure drop

Δp_{wet} : wet pressure drop

κ : Curvature of interface

μ : Dynamic viscosity

ν : Kinematic viscosity

ρ : Density

σ : Surface tension

ω : Specific rate of dissipation

Subscripts

G : Gas

n : Normalized value

L : Liquid

T : Turbulent

Abbreviations

CFD : Computational Fluid Dynamics

CFL : Courant–Friedrichs–Lewy

CO_2 : Carbon dioxide

CO_2BOL: CO_2-binding organic liquids

EEMPA: N-(2-ethoxyethyl)-3-morpholinopropan-1-amine

MEA : Monoethanolamine

PNNL : Pacific Northwest National Laboratory

REU : Representative elementary unit

TPMS : Triply periodic minimal surface

VOF : Volume of fluid

REFERENCES

1. *Inventory of U.S. Greenhouse Gas Emissions and Sinks: 1990-2018*, U.S.E.P. Agency, Editor. 2020, U.S. Environmental Protection Agency,.
2. Yoro, K.O. and M.O. Daramola, *Chapter 1 - CO2 emission sources, greenhouse gases, and the global warming effect*, in *Advances in Carbon Capture*, M.R. Rahimpour, M. Farsi, and M.A. Makarem, Editors. 2020, Woodhead Publishing. p. 3-28.
3. Razi, N., O. Bolland, and H. Svendsen, *Review of design correlations for CO2 absorption into MEA using structured packings.* International Journal of Greenhouse Gas Control, 2012. **9**(0): p. 193-219.
4. Rochelle, G.T., *Amine Scrubbing for CO2 Capture.* Science, 2009. **325**(5948): p. 1652-1654.
5. Spiegel, L. and W. Meier, *Distillation Columns with Structured Packings in the Next Decade.* Chemical Engineering Research and Design, 2003. **81**(1): p. 39-47.
6. Figueroa, J.D., et al., *Advances in CO2 capture technology—The U.S. Department of Energy's Carbon Sequestration Program.* International Journal of Greenhouse Gas Control, 2008. **2**(1): p. 9-20.
7. Raynal, L. and A. Royon-Lebeaud, *A multi-scale approach for CFD calculations of gas–liquid flow within large size column equipped with structured packing.* Chemical Engineering Science, 2007. **62**(24): p. 7196-7204.
8. Ngo, T.D., et al., *Additive manufacturing (3D printing): A review of materials, methods, applications and challenges.* Composites Part B: Engineering, 2018. **143**: p. 172-196.
9. Nguyen, D., et al., *3D Printed Polymer Composites for CO2 Capture.* Industrial & Engineering Chemistry Research, 2019. **58**(48): p. 22015-22020.
10. Sarma, M., et al., *Investigation of chemical stabilities and contact angle of 3D printed polymers with CO2 capture solvents to enhance absorber performance.* International Journal of Greenhouse Gas Control, 2021. **111**.
11. Tijing, L.D., et al., *3D printing for membrane separation, desalination and water treatment.* Applied Materials Today, 2020. **18**.
12. Reitze, A., M. Grünewald, and J. Riese, *Characterization of Liquid-Phase Distribution in 3D Printed Structured Packings with an Enclosed Column Wall.* Industrial & Engineering Chemistry Research, 2021. **61**(1): p. 740-746.
13. Stolaroff, J.K. *High-efficiency, integrated reactors for sorbents, solvents, and membranes using additive manufacturing*. in *2017 NETL CO2 Capture Technology Project Review Meeting*. 2017. Pittsburgh, PA: National Energy Technology Laboratory.
14. Gładyszewski, K. and M. Skiborowski, *Additive manufacturing of packings for rotating packed beds.* Chemical Engineering and Processing - Process Intensification, 2018. **127**: p. 1-9.
15. Bolton, S., et al., *3D printed structures for optimized carbon capture technology in packed bed columns.* Separation Science and Technology, 2019. **54**(13): p. 2047-2058.
16. Moore, T., et al., *Advanced absorber heat integration via heat exchange packings.* AIChE Journal, 2021.
17. Qu, S., J. Ding, and X. Song, *Achieving Triply Periodic Minimal Surface Thin-Walled Structures by Micro Laser Powder Bed Fusion Process.* Micromachines (Basel), 2021. **12**(6).
18. Dudukovic, N.A., et al., *Cellular fluidics.* Nature, 2021. **595**(7865): p. 58-65.
19. Sreedhar, N., et al., *Mass transfer analysis of ultrafiltration using spacers based on triply periodic minimal surfaces: Effects of spacer design, directionality and voidage.* Journal of Membrane Science, 2018. **561**: p. 89-98.
20. Chandrasekaran, G., *3D Printed Heat Exchangers: An Experimental Study*, in *Mechanical Engineering*. 2018, Arizona State University: Tempe, AZ, USA. p. 61.
21. Zimmer, A., et al., *Effect of Manufacturing Techniques in Pressure Drop on Triple Periodical Minimal Surface Packings* Chemie Ingenieur Technik, 2021. **93**(6): p. 967-973.
22. Ataki, A. and H.J. Bart, *Experimental and CFD simulation study for the wetting of a structured packing element with liquids.* Chemical Engineering & Technology, 2006. **29**(3): p. 336-347.

23. Tsai, R.E., *Mass Transfer Area of Structured Packing*, in *Chemical Engineering*. 2010, The University of Texas at Austin: Austin, TX. p. 400.
24. Bradtmöller, C., et al., *Influence of Viscosity on Liquid Flow Inside Structured Packings.* Industrial & Engineering Chemistry Research, 2015. **54**(10): p. 2803-2815.
25. Singh, R.K., J.E. Galvin, and X. Sun, *Multiphase flow studies for microscale hydrodynamics in the structured packed column.* Chemical Engineering Journal, 2018. **353**: p. 949-963.
26. Haroun, Y., L. Raynal, and P. Alix, *Prediction of effective area and liquid hold-up in structured packings by CFD.* Chemical Engineering Research and Design, 2014. **92**(11): p. 2247-2254.
27. Fu, Y., et al., *Investigation of countercurrent flow profile and liquid holdup in random packed column with local CFD data.* Chemical Engineering Science, 2020. **221**.
28. Fu, Y., et al., *The influence of random packed column parameters on the liquid holdup and interfacial area.* AIChE Journal, 2022.
29. Janzen, A., et al., *Investigation of liquid flow morphology inside a structured packing using X-ray tomography.* Chemical Engineering Science, 2013. **102**: p. 451-460.
30. Tsai, R.E., et al., *Influence of viscosity and surface tension on the effective mass transfer area of structured packing.* Energy Procedia, 2009. **1**(1): p. 1197-1204.
31. Singh, R.K., J.E. Galvin, and X. Sun, *Three-dimensional simulation of rivulet and film flows over an inclined plate: Effects of solvent properties and contact angle.* Chemical Engineering Science, 2016. **142**: p. 244-257.
32. Xu, Z., et al., *Direct Effect of Solvent Viscosity on the Physical Mass Transfer for Wavy Film Flow in a Packed Column.* Industrial & Engineering Chemistry Research, 2019. **58**(37): p. 17524-17539.
33. Song, D., A.F. Seibert, and G.T. Rochelle, *Mass Transfer Parameters for Packings: Effect of Viscosity.* Industrial & Engineering Chemistry Research, 2018. **57**(2): p. 718-729.
34. Jammula, A.K., *New Liquid Holdup, Load Point and Flooding Velocity Models in Different Regions of Operations for a Structured Packed Column*, in *Chemical Engineering*. 2014, Oklahoma State University: Stillwater, OK p. 164.
35. Sebastia-Saez, D., et al., *Meso-scale CFD study of the pressure drop, liquid hold-up, interfacial area and mass transfer in structured packing materials.* International Journal of Greenhouse Gas Control, 2015. **42**: p. 388-399.
36. Olenberg, A. and E.Y. Kenig, *Numerical investigation of liquid flow morphology in structured packings.* Chemical Engineering Science, 2020. **219**: p. 115559.
37. Said, W., M. Nemer, and D. Clodic, *Modeling of dry pressure drop for fully developed gas flow in structured packing using CFD simulations.* Chemical Engineering Science, 2011. **66**(10): p. 2107-2117.
38. Tsai, R.E., et al., *A dimensionless model for predicting the mass-transfer area of structured packing.* AIChE Journal, 2011. **57**(5): p. 1173-1184.
39. Bravo, J.L., A.A. Patwardhan, and T.F. Edgar, *Influence of effective interfacial areas in the operation and control of packed distillation columns.* Industrial & Engineering Chemistry Research, 1992. **31**(2): p. 604-608.
40. Billet, R. and M. Schultes, *Prediction of Mass Transfer Columns with Dumped and Arranged Packings.* Chemical Engineering Research and Design, 1999. **77**(6): p. 498-504.
41. Fourati, M., V. Roig, and L. Raynal, *Experimental study of liquid spreading in structured packings.* Chemical Engineering Science, 2012. **80**: p. 1-15.
42. Snoeijer, J.H. and B. Andreotti, *A microscopic view on contact angle selection.* Physics of Fluids, 2008. **20**(5): p. 057101.
43. Fan, L.T., et al., *Contact Angle of Ethanol and n-Propanol Aqueous Solutions on Metal Surfaces.* Chemical Engineering & Technology, 2011. **34**(9): p. 1535-1542.
44. Wenzel, R.N., *Resistance of solid surfaces to wetting by water.* Industrial & Engineering Chemistry, 1936. **28**(8): p. 988-994.
45. Nicolaiewsky, E.M.A. and J.R. Fair, *Liquid Flow over Textured Surfaces. 1. Contact Angles.* Industrial & Engineering Chemistry Research, 1998. **38**(1): p. 284-291.

46. Singh, R.K., J.E. Galvin, and X. Sun, *Hydrodynamics of the rivulet flow over corrugated sheet used in structured packings.* International Journal of Greenhouse Gas Control, 2017. **64**: p. 87-98.
47. Zisman, W.A., *Relation of the Equilibrium Contact Angle to Liquid and Solid Constitution*, in *Contact Angle, Wettability, and Adhesion*. 1964, American Chemical Society. p. 1-51.
48. Shi, M.G. and A. Mersmann, *Effective interfacial area in packed columns.* German chemical engineering, 1985. **8**(2): p. 87-96.
49. Femmer, T., A.J.C. Kuehne, and M. Wessling, *Estimation of the structure dependent performance of 3-D rapid prototyped membranes.* Chemical Engineering Journal, 2015. **273**: p. 438-445.
50. Iyer, J., et al., *Heat transfer and pressure drop characteristics of heat exchangers based on triply periodic minimal and periodic nodal surfaces.* Applied Thermal Engineering, 2022. **209**.
51. CD-adapco *STAR-CCM+ 13.04 User Guide*. 2018.
52. Hirt, C.W. and B.D. Nichols, *Volume of fluid (VOF) method for the dynamics of free boundaries.* Journal of Computational Physics, 1981. **39**(1): p. 201-225.
53. Brackbill, J.U., D.B. Kothe, and C. Zemach, *A continuum method for modeling surface tension.* Journal of Computational Physics, 1992. **100**(2): p. 335-354.
54. Joly, J.F., et al., *CFD Applied to Process Development in the Oil and Gas Industry – A Review.* Oil & Gas Science and Technology – Revue d'IFP Energies nouvelles, 2015. **71**(3).
55. Raynal, L., C. Boyer, and J.-P. Ballaguet, *Liquid Holdup and Pressure Drop Determination in Structured Packing with CFD Simulations.* The Canadian Journal of Chemical Engineering, 2004. **82**(5): p. 871-879.
56. Höhne, T. and J.-P. Mehlhoop, *Validation of closure models for interfacial drag and turbulence in numerical simulations of horizontal stratified gas–liquid flows.* International Journal of Multiphase Flow, 2014. **62**(0): p. 1-16.
57. Singh, R.K., C. Wang, and Z. Xu, *Residence time distribution in a structured packing unit for monitoring aerosol emissions.* International Journal of Greenhouse Gas Control, 2018. **79**: p. 181-192.
58. Menter, F.R., *Two-equation eddy-viscosity turbulence models for engineering applications.* AIAA Journal, 1994. **32**(8): p. 1598-1605.
59. Schwarz, H.A., *Gesammelte mathematische abhandlungen*. 1890, Berlin: J. Springer.
60. Al-Ketan, O. and R.K. Abu Al-Rub, *Multifunctional Mechanical Metamaterials Based on Triply Periodic Minimal Surface Lattices.* Advanced Engineering Materials, 2019. **21**(10).
61. Fu, Y., et al., *Absorber Column CFD model validation against PNNL's device-scale absorber column on the LCFS unit*. 2020, Pacific Northwest National Laboratory: United States. p. 1 - 57.
62. Lail, M., J. Tanthana, and L. Coleman, *Non-Aqueous Solvent (NAS) CO2 Capture Process.* Energy Procedia, 2014. **63**: p. 580-594.
63. DOE/NETL, *Carbon Dioxide Capture Handbook*, DOE/NETL, Editor. 2015, National Energy Technology Laboratory. p. 116.
64. Whyatt, G.A., et al., *Measuring Nitrous Oxide Mass Transfer into Non-Aqueous CO2BOL CO2 Capture Solvents.* Industrial & Engineering Chemistry Research, 2016. **55**(16): p. 4720-4725.
65. Mathias, P.M., et al., *Improving the regeneration of CO2-binding organic liquids with a polarity change.* Energy & Environmental Science, 2013. **6**(7).
66. Zheng, R.F., et al., *A single-component water-lean post-combustion CO2 capture solvent with exceptionally low operational heat and total costs of capture – comprehensive experimental and theoretical evaluation.* Energy & Environmental Science, 2020. **13**(11): p. 4106-4113.
67. Niegodajew, P., et al., *A study of liquid spreading in laboratory scale random packing column with an optical method supplemented with liquid holdup characteristics.* Experimental Thermal and Fluid Science, 2018. **96**: p. 162-168.
68. Singh, R.K., et al., *Hydrodynamics of countercurrent flows in a structured packed column: Effects of initial wetting and dynamic contact angle.* Chemical Engineering Journal, 2020. **398**.

69. Singh, R.K., et al., *Device-scale CFD study for mass transfer coefficient and effective mass transfer area in packed column*. 2018, ; Pacific Northwest National Lab. (PNNL), Richland, WA (United States). p. Medium: ED; Size: 54 p.
70. Singh, R.K., et al., *Breakup of a liquid rivulet falling over an inclined plate: Identification of a critical Weber number.* Physics of Fluids, 2017. **29**(5): p. 052101.
71. Subramanian, K. and G. Wozny, *Analysis of Hydrodynamics of Fluid Flow on Corrugated Sheets of Packing.* International Journal of Chemical Engineering, 2012. **2012**: p. 13.
72. Wang, C., et al., *Beyond the standard two-film theory: Computational fluid dynamics simulations for carbon dioxide capture in a wetted wall column.* Chemical Engineering Science, 2018. **184**: p. 103-110.
73. Wang, C., et al., *Hierarchical calibration and validation framework of bench-scale computational fluid dynamics simulations for solvent-based carbon capture. Part 2: Chemical absorption across a wetted wall column.* Greenhouse Gases: Science and Technology, 2018. **8**(1): p. 150-160.
74. Billet, R. and M. Schultes, *Modelling of pressure drop in packed columns.* Chemical Engineering & Technology, 1991. **14**(2): p. 89-95.
75. Mackowiak, J., *Fluid Dynamics of Packed Columns*. 2010, Berlin: Springer-Verlag.
76. Schoenmakers, H. and L. Spiegel, *Chapter 10 - Laboratory Distillation and Scale-up*, in *Distillation*, A. Górak and Ž. Olujić, Editors. 2014, Academic Press: Boston. p. 319-339.
77. Stichlmair, J., J.L. Bravo, and J.R. Fair, *General model for prediction of pressure drop and capacity of countercurrent gas/liquid packed columns.* Gas Separation & Purification, 1989. **3**(1): p. 19-28.
78. Ergun, S., *Fluid flow through packed columns.* Fluid Flow Through Packed Columns, 1952. **48**: p. 89-94.
79. Danckwerts, P.V., *The reaction of CO2 with ethanolamines.* Chemical Engineering Science, 1979. **34**(4): p. 443-446.
80. Siminiceanu, I., et al., *Measuring the Effective Mass Transfer Area of a Structured Packing by a Chemical Method.* Revista De Chimie, 2008. **59**(10): p. 1117-1121.
81. Buchanan, J.E., *Pressure Gradient and Liquid Holdup in Irrigated Packed Towers.* Industrial & Engineering Chemistry Fundamentals, 1969. **8**(3): p. 502-511.
82. Finn, J.R. and J.E. Galvin, *Calibration of drag models for mesoscale simulation of gas–liquid flow through packed beds.* Chemical Engineering Science, 2017. **172**: p. 722-730.
83. Maćkowiak, J., *Pressure Drop of Dry Packed Columns*, in *Fluid Dynamics of Packed Columns: Principles of the Fluid Dynamic Design of Columns for Gas/Liquid and Liquid/Liquid Systems*. 2010, Springer Berlin Heidelberg: Berlin, Heidelberg. p. 123-174.
84. Hanley, B., *On packed column hydraulics.* AIChE Journal, 2012. **58**(6): p. 1671-1682.

Table 1: Physical properties of solvents used in flow simulations at 25°C.

Solvent	$\boldsymbol{\rho_L}$ (kg/m^3)	$\boldsymbol{\mu_L}$ (*m*Pas)	**σ** (*m*N/m)	**Ka**
Water	997	0.97	72.80	3538
40MEA (40% MEA by weight)	1053	3.791	54.80	443
EEMPA	938	7.083	34.40	116

Table 2: Correlations for wet pressure drop in the packed column.

Model	Expression for $\left(\Delta p_{wet}/H\right)$	Remark
Billet and Schultes [74]	$f(S)\left(\frac{\varepsilon}{\varepsilon - h_L}\right)^{3/2}\frac{\Delta p_0}{H}$ Here, $f(S)=\exp\left(\mathrm{Re_L}/200\right)$ and $\mathrm{Re}_L = u_L/a_p\nu_L$, ν_L is kinemetic viscosity. $\Delta p_0/H$ from Equation **Error! Reference source not found.**.	Random packed column
Stichlmair model [77]	$\left(1+\frac{h_L}{1-\varepsilon}\right)^{(2+c)/3}\left(\frac{\varepsilon}{\varepsilon - h_L}\right)^{4.65}\frac{\Delta p_0}{H}$ Here, $c=-\left\{\frac{C_1}{\mathrm{Re_G}}+\frac{C_2}{2\cdot\mathrm{Re_G^{0.5}}}\right\}\frac{1}{\psi_0}$, $\Delta p_0/H$ from Equation **Error! Reference source not found.**, C_1=5, C_2=3	Structured packed column
Maćkowiak model [81]	$\left(1-\frac{2\cdot h_L}{a_p\cdot d_h}\right)^{-5}\frac{\Delta p_0}{H}$ $\Delta p_0/H$ from Equation **Error! Reference source not found.**	Irrigation channel model for Random packed column

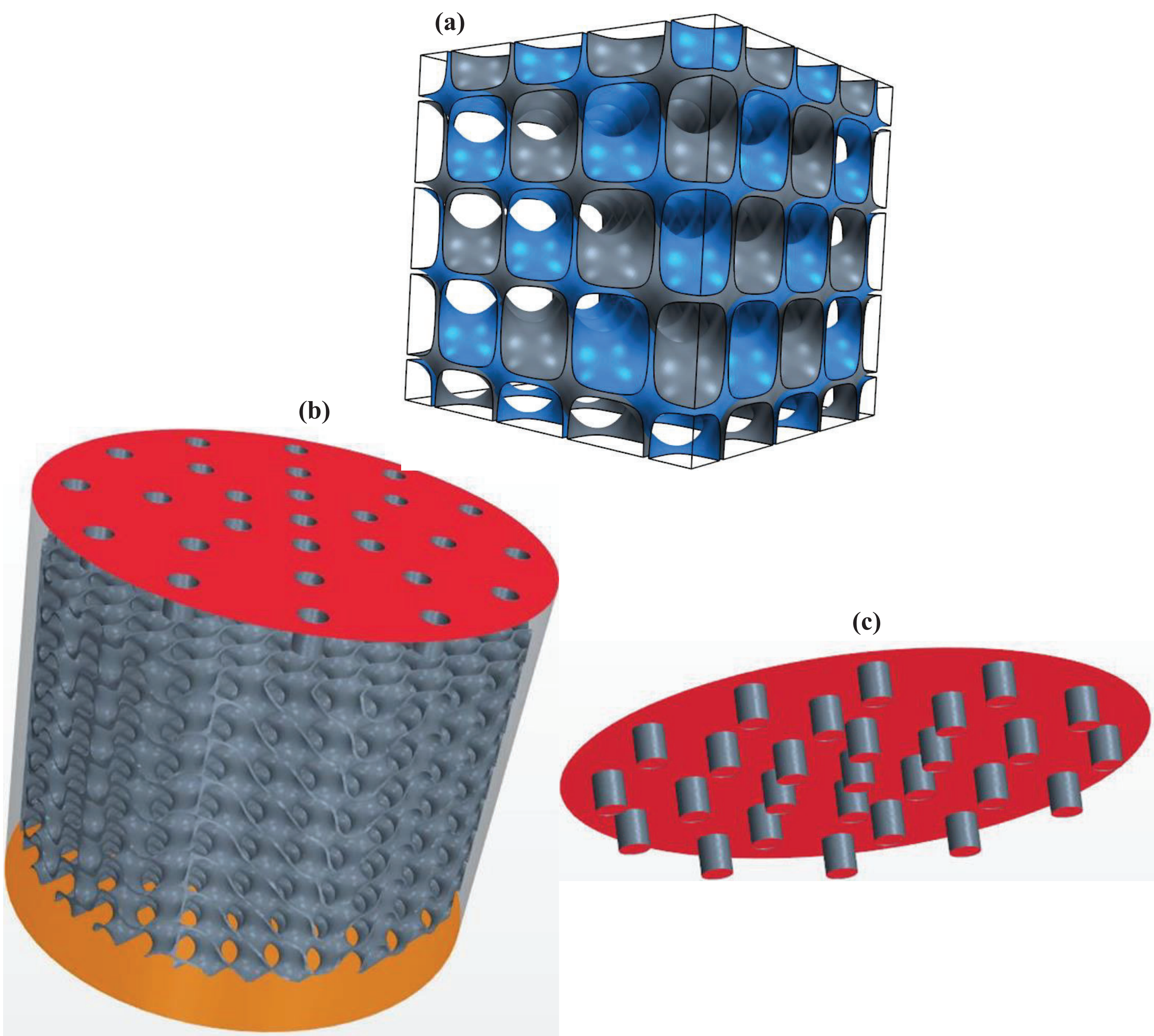

Figure 1(color online): (a) Three-dimensional view of Schwarz-D cells showing two disjointed flow domains depicted in distinct colors. (b) Three-dimensional view of the computational domain showing the Schwarz-D column having a 80 mm diameter and 75 mm height. (c) The arrangement of dripping points at the top of the column. The liquid is fed to the column through these dripping points.

(a)

(b)

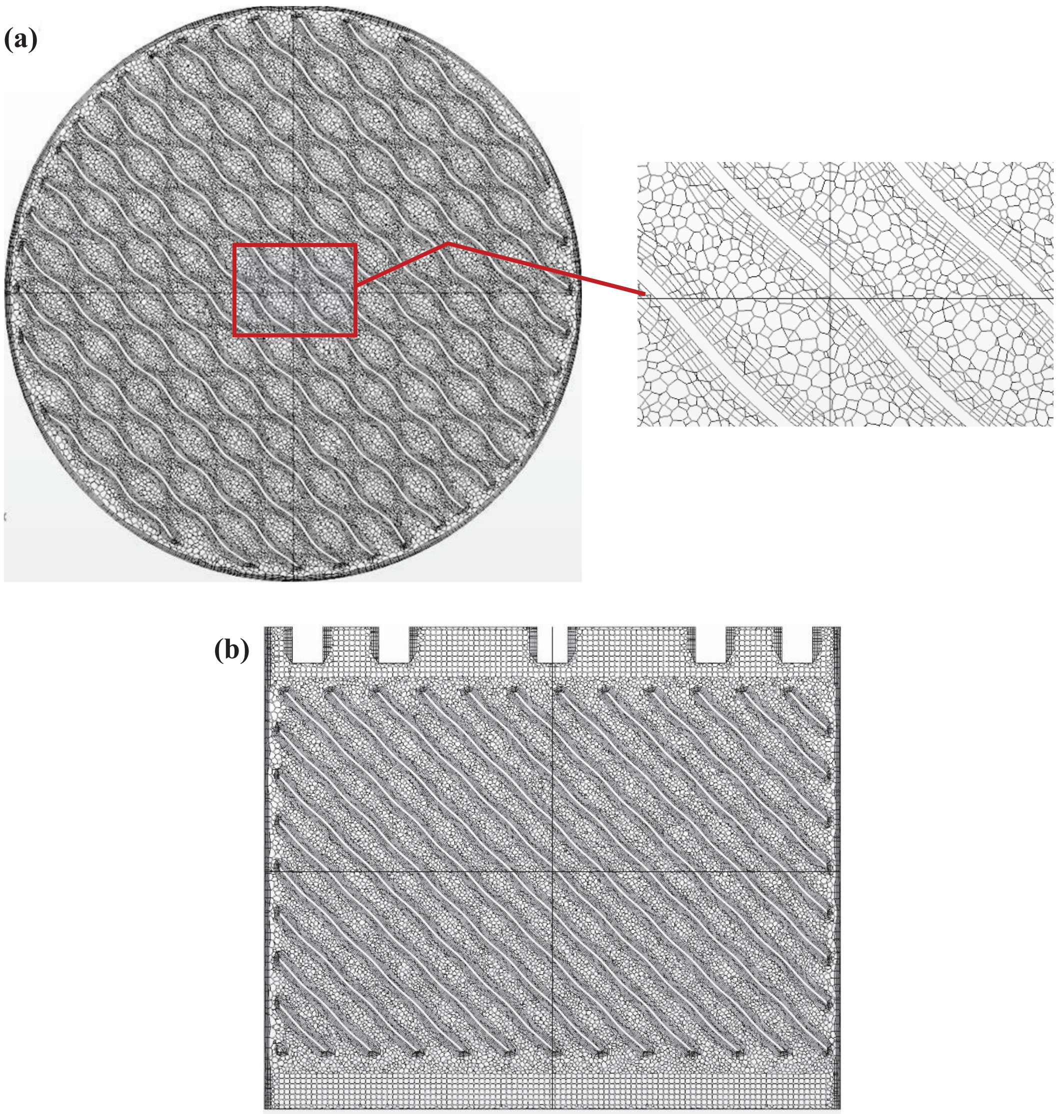

Figure 2: Meshing of the flow domain (a) cross-section of column and (b) central vertical plane shows the nonuniform mesh used in the discretization of flow domain. Very fine mesh is used near the sheet where the gas-liquid interface may appear (see the exploded view in Figure (a)).

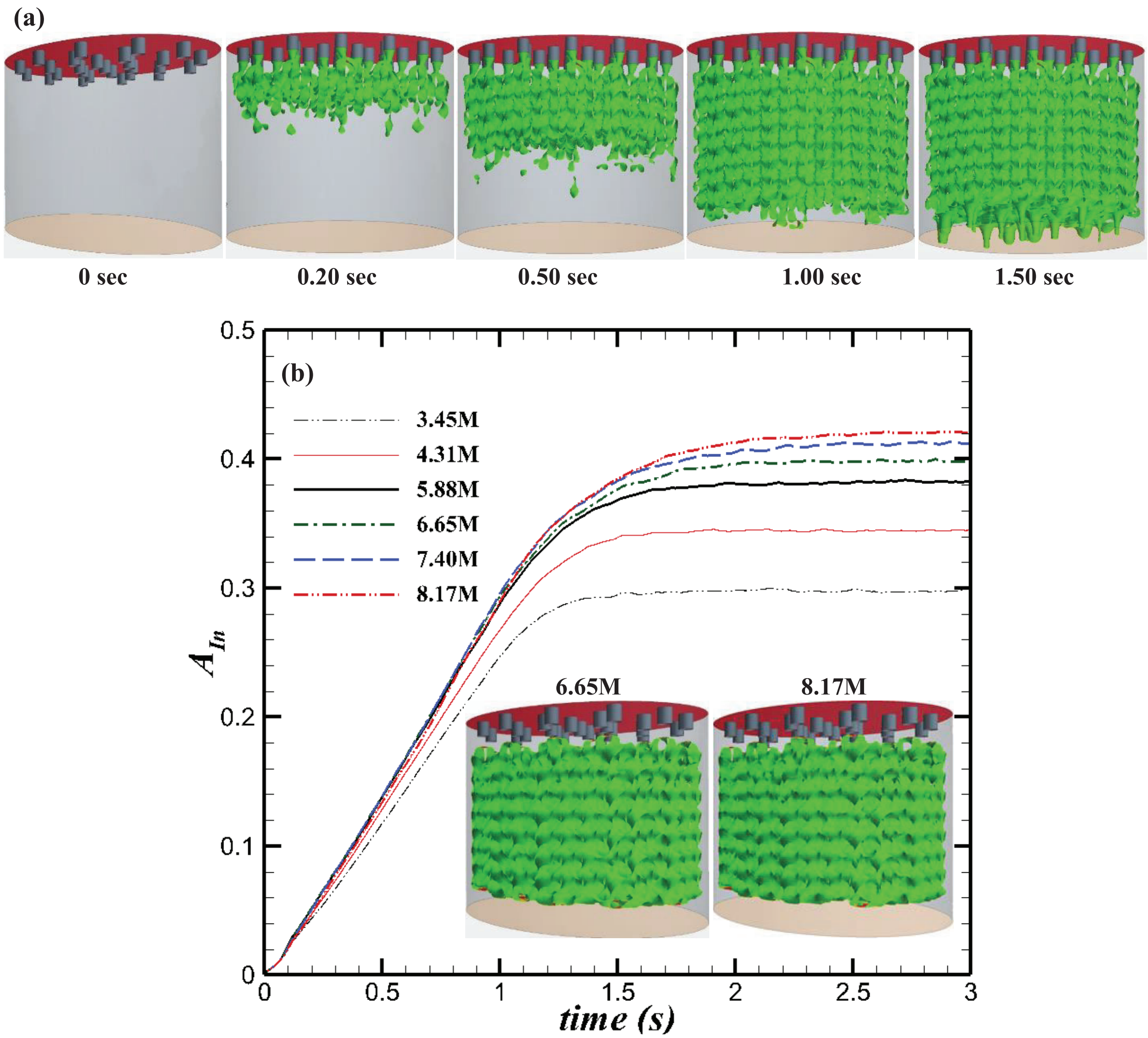

Figure 3 (color online): (a) Snapshots of gas-liquid interface at different time instants in Schwarz-D packed column for EEMPA with $\gamma = 30°$, $q_L = 180m^3/m^2h$, $F_G^2 = 1.18$ Pa and 6.65 M cells. (b) Plot for temporal evolution of the normalized interfacial area (A_{In}) for same case but different grid resolutions. Snapshots of interface at 3 sec in the insets shows almost identical shape at both grid resolutions.

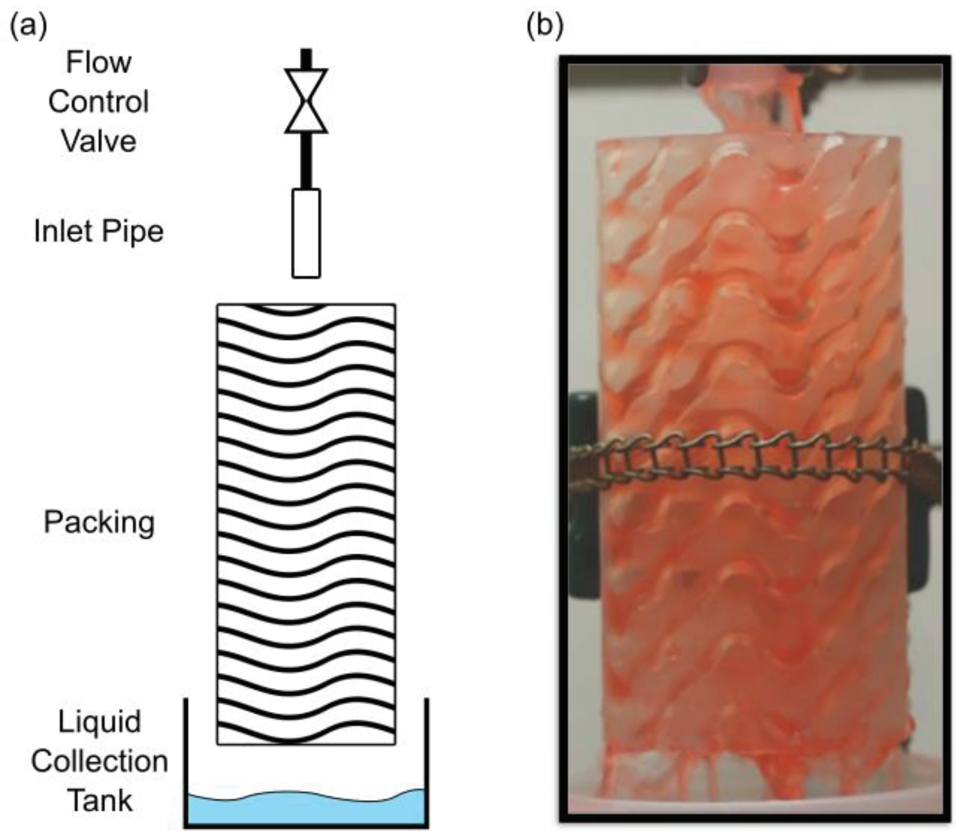

Figure 4: (a) Sketch of the experimental setup used to measure the liquid holdup in the packed column. (b) Water with red dye was used to visualize the flow in the packed column

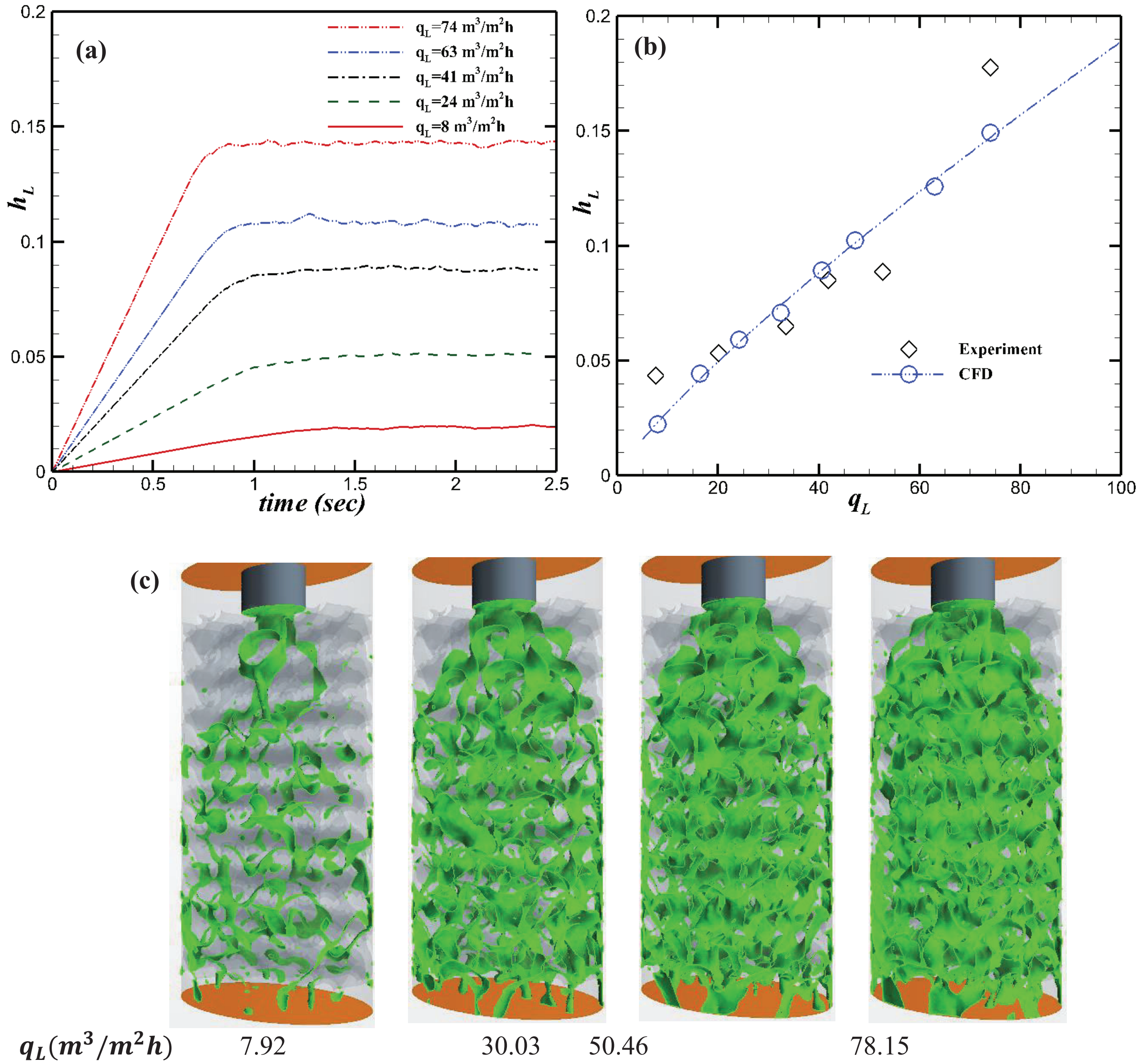

Figure 5 (color online): (a) Temporal evaluation of the liquid holdup in the Schwarz-D column at different liquid loads. (b) Comparison of the predicted liquid holdup in the TPMS region with corresponding experimental value under same condition. (c) Snapshots of the pseudo-steady shape of the gas-liquid interface for water at $\gamma = 70°$ and different q_L values.

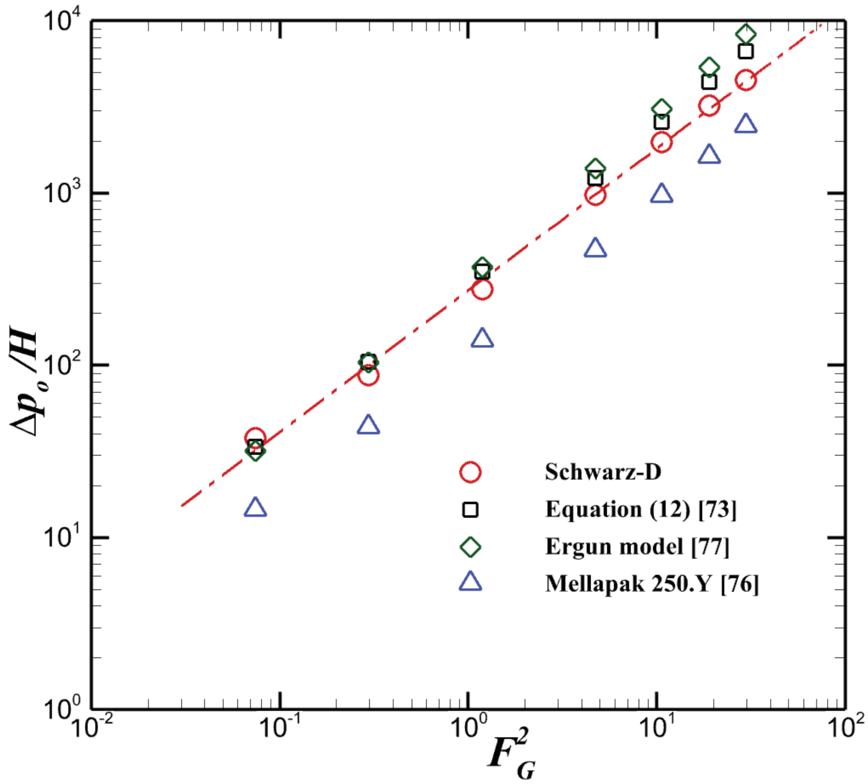

Figure 6 (color online): Variation of the dry pressure drop per unit length with gas capacity factors in the Schwarz-D column.

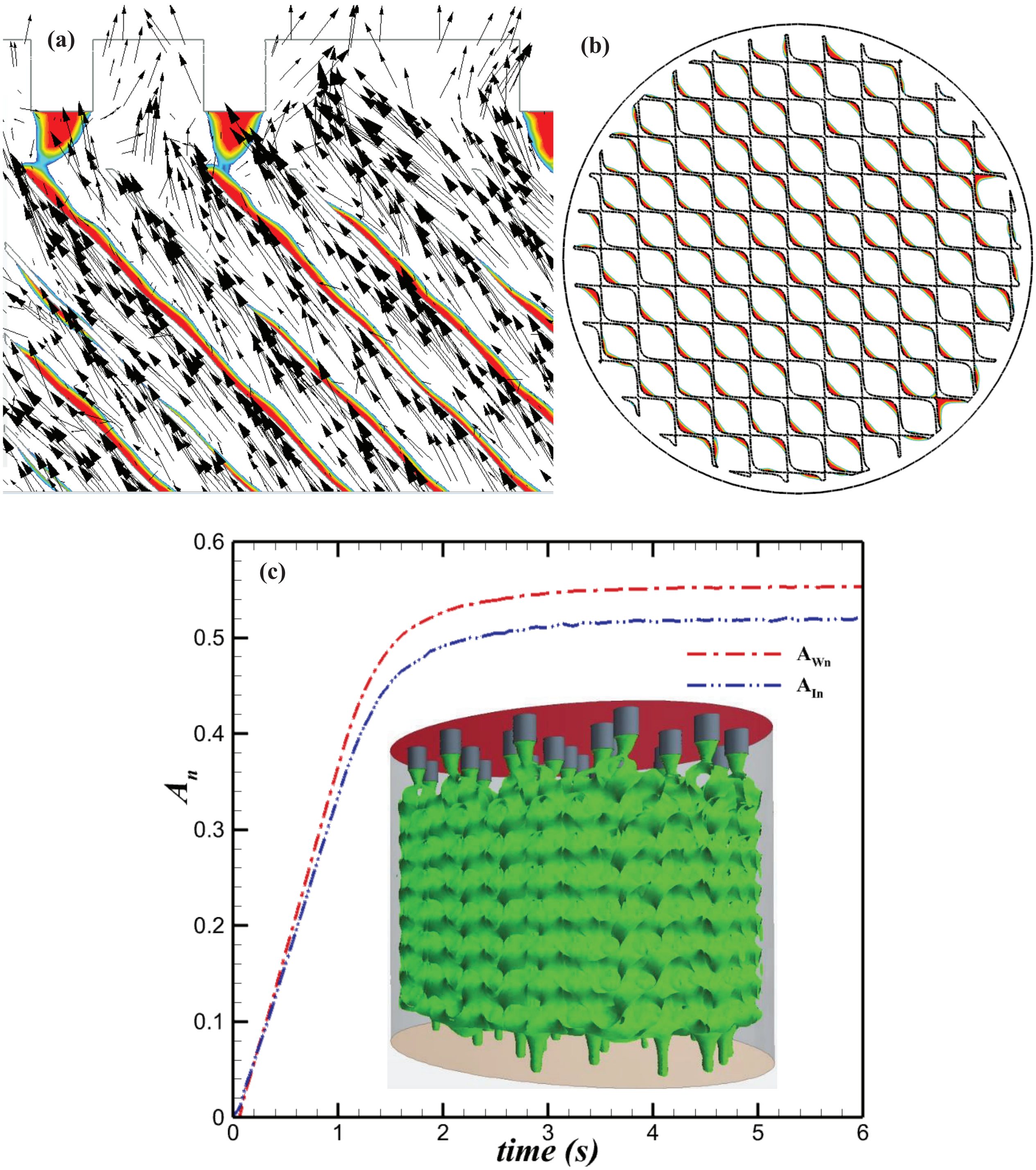

Figure 7 (color online): (a) Exploded view at the top of the vertical x-z plane shows the countercurrent flow in the Schwarz-D column. Red color delineates the solvent flow whereas velocity vector shows upward gas flow. (b) Solvent distribution at a cross-sectional plane in the middle of column. (c) Temporal evolution of the interfacial and wetted areas in a for EEMPA at $q_L = 180\, m^3/m^2h$, $F_G^2 = 1.18\, Pa$ and $\gamma = 10°$. The pseudo-steady state was considered when both areas become nearly constant. Inset of Figure (b) shows the gas-liquid interface in the column at t = 6 s.

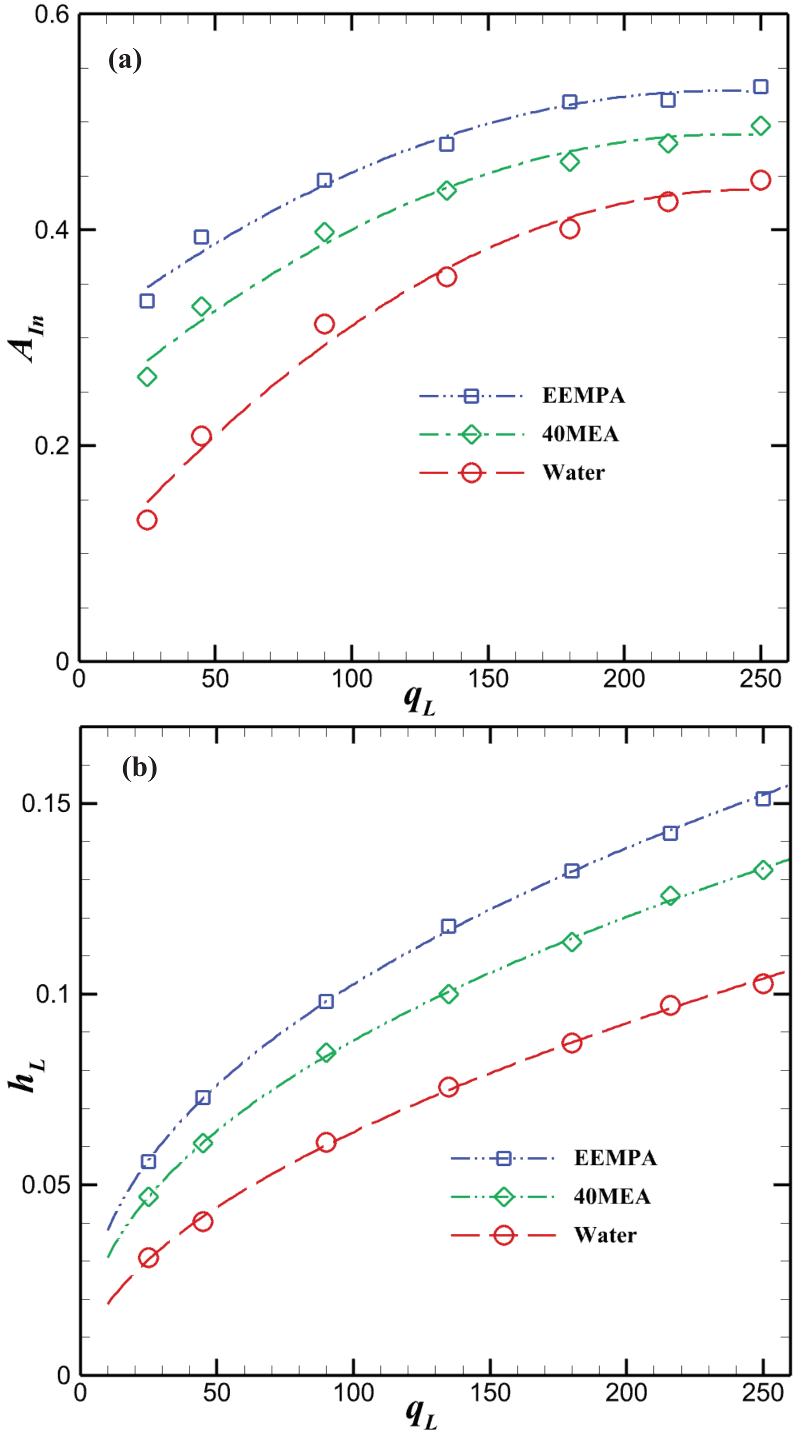

Figure 8 (color online): Effect of liquid loads on the (a) interfacial area and (b) liquid holdup in the Schwarz-D packing at $\gamma = 10°$, $F_G^2 = 1.18\ Pa$ for three solvents. EEMPA shows the highest value of the interfacial area and liquid holdup at all values of liquid loads.

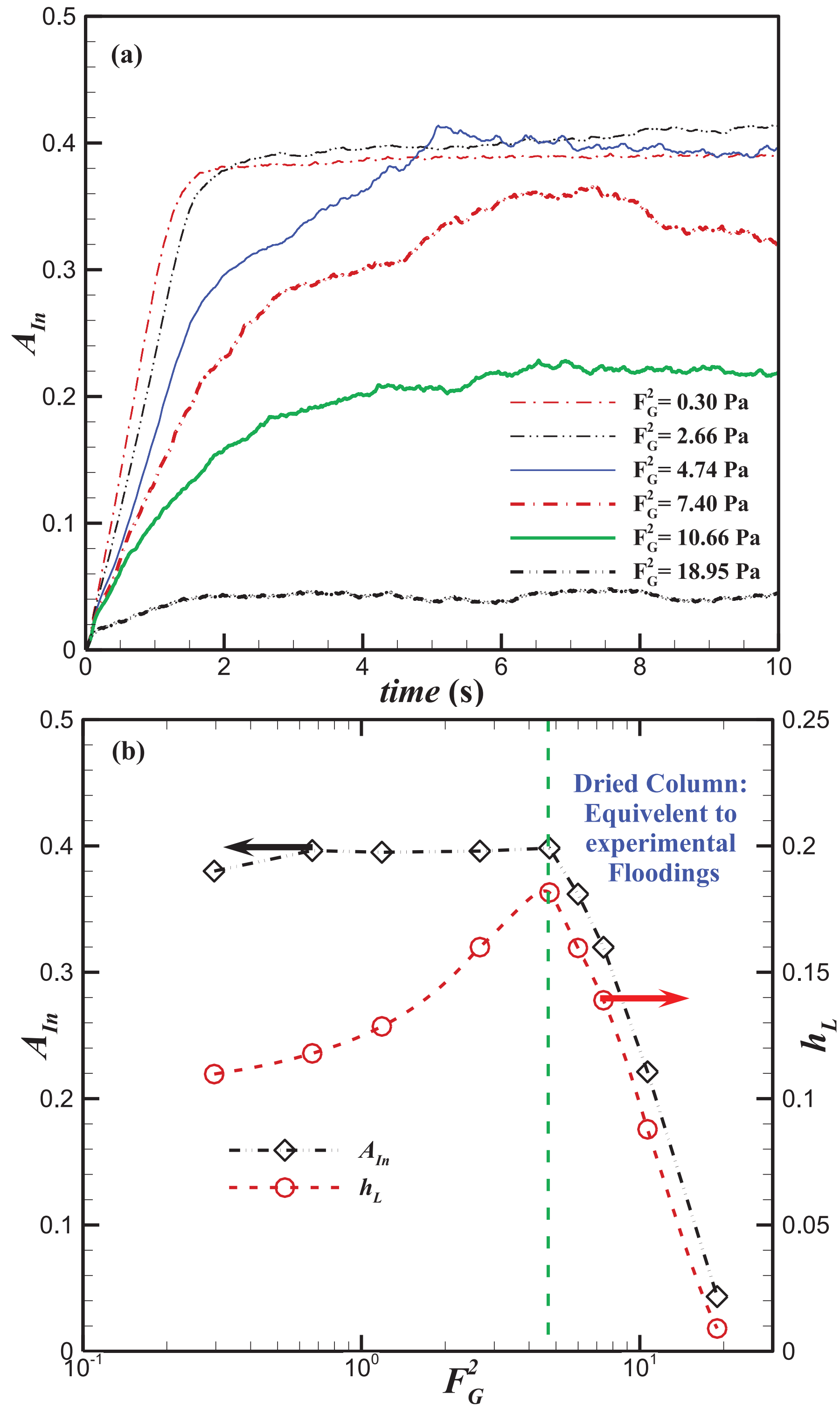

Figure 9 (color online): (a) Temporal evolution of the interfacial area (A_{In}) for EEMPA at $q_L = 180\ m^3/m^2h, \gamma = 30°$ and different value of F_G^2. (b) Variation of the interfacial area and liquid holdup with gas capacity factor for same cases when simulation achieves the pseudo steady state. The right side of the vertical dotted line is equivalent to flooding to flooding conditions.

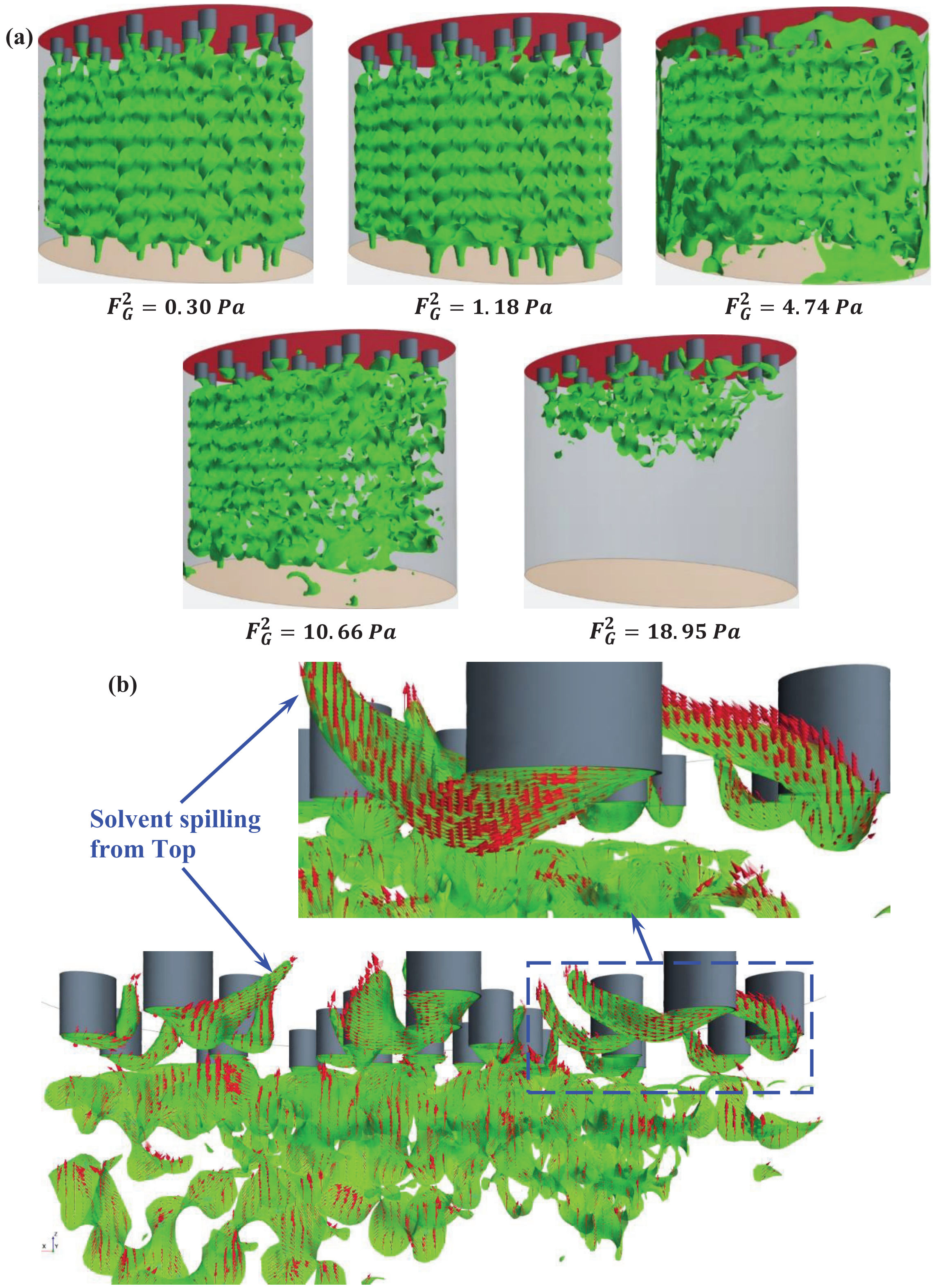

Figure 10 (color online): (a) Snapshots of the pseudo steady shapes of interface factor for EEMPA at $q_L = 180\ m^3/m^2h$, $\gamma = 30°$ and different value of F_G^2. (b) velocity vector at the interface shows the upward flow of solvent at the top of the column at $F_G^2 = 18.95\ Pa$.

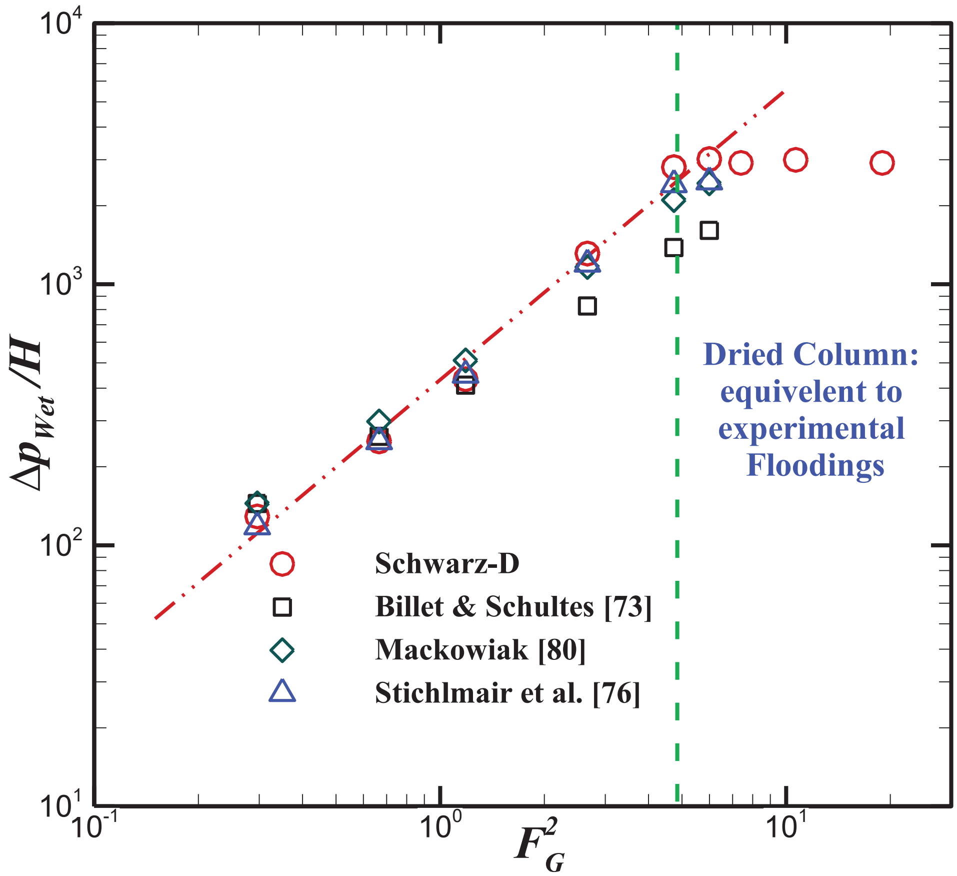

Figure 11 (color online): Variation of the wet pressure drop per unit length in the column with gas capacity factor for EEMPA at $q_L = 180\ m^3/m^2h$ and $\gamma = 30°$. The CFD predicted value matches well with correlations at lower gas capacity factor i.e. loading and preloading regime. The right side of vertical green dashed line represents dried column which is equivalent to experimental flooding conditions.

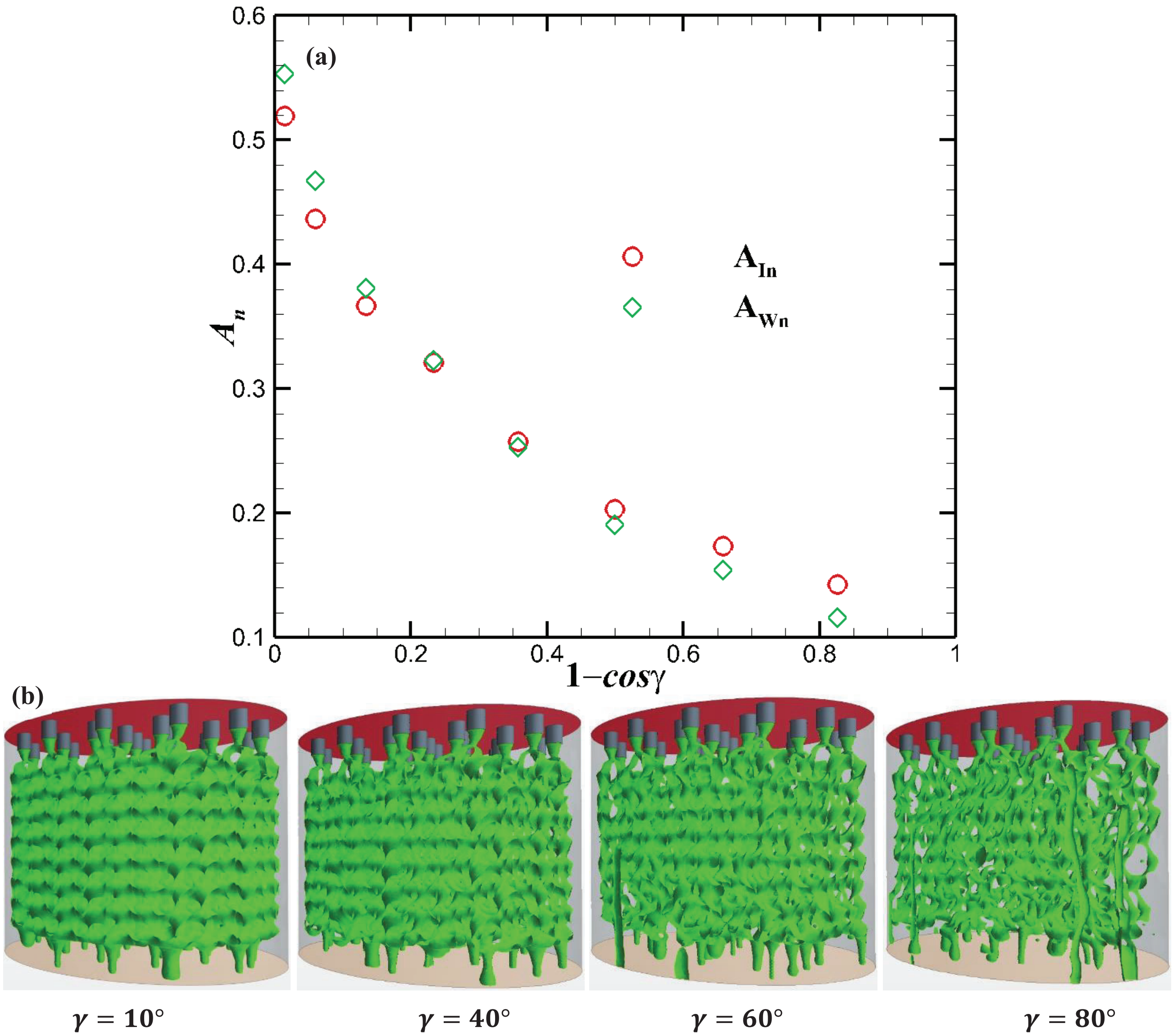

Figure 12 (Color online): (a) variation of normalized wetted (A_{wn}) and interfacial (A_{In})areas with contact angles (γ) for EEMPA at $q_L = 180\ m^3/m^2h$ and $F_G^2 = 1.18\ Pa$. (b) Snapshot of the gas-liquid interface at different contact angles. Flow regime transition, i.e. rivulet to film begins around $\gamma = 40°$.

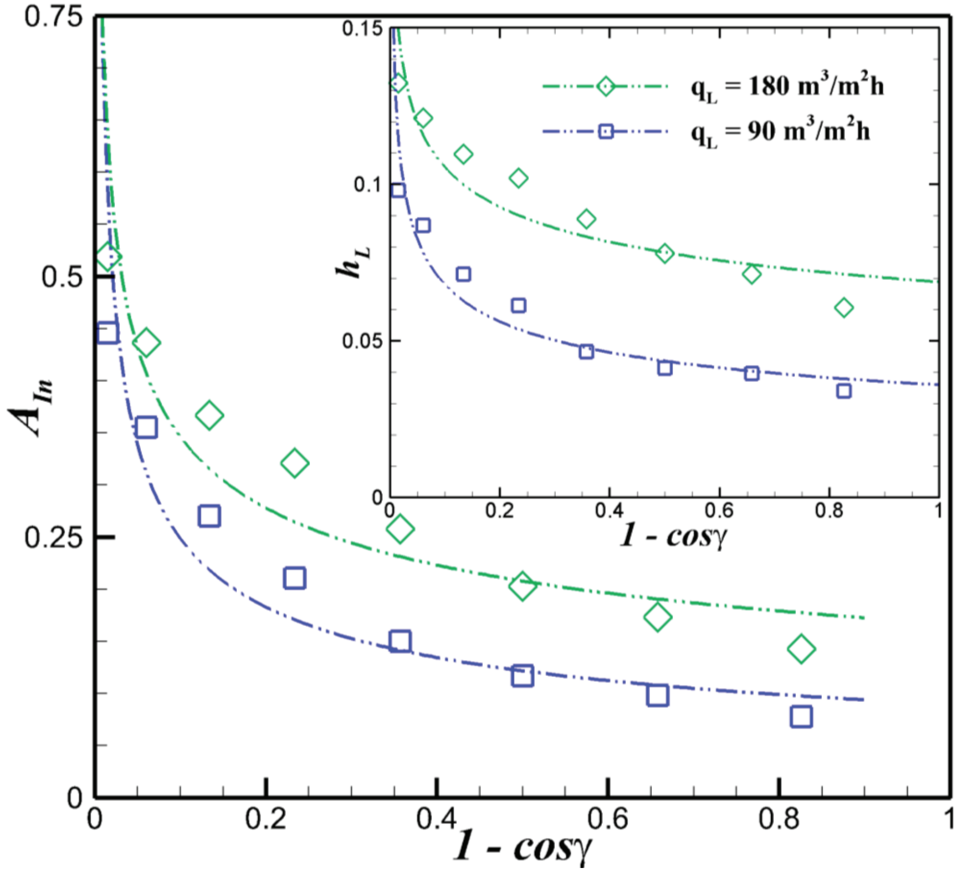

Figure 13 (color online): Variation of A_{In} with γ in the Schwarz-D column for EEMPA solvent at $F_G^2 = 1.18\, Pa$ and two liquid loads. Inset shows the variation of h_L with γ for same case. Both quantities decrease with increased value of contact angle.